Hindawi
Complexity
Volume 2020, Article ID 8541432, 18 pages
https://doi.org/10.1155/2020/8541432

Research Article

Spatiotemporal Patterns Formed by a Discrete Nutrient-Phytoplankton Model with Time Delay

Feifan Zhang, Wenjiao Zhou, Lei Yao, Xuanwen Wu, and Huayong Zhang

Research Center for Engineering Ecology and Nonlinear Science, North China Electric Power University, Beijing 102206, China

Correspondence should be addressed to Huayong Zhang; rceens@ncepu.edu.cn

Received 20 September 2019; Revised 27 November 2019; Accepted 11 December 2019; Published 9 January 2020

Academic Editor: Eric Campos-Canton

In this research, a continuous nutrient-phytoplankton model with time delay and Michaelis–Menten functional response is discretized to a spatiotemporal discrete model. Around the homogeneous steady state of the discrete model, Neimark–Sacker bifurcation and Turing bifurcation analysis are investigated. Based on the bifurcation analysis, numerical simulations are carried out on the formation of spatiotemporal patterns. Simulation results show that the diffusion of phytoplankton and nutrients can induce the formation of Turing-like patterns, while time delay can also induce the formation of cloud-like pattern by Neimark–Sacker bifurcation. Compared with the results generated by the continuous model, more types of patterns are obtained and are compared with real observed patterns.

1. Introduction

Phytoplankton is the main producer of aquatic ecosystems and forms the basis of food webs [1]. The growth of phytoplankton can determine the behavioral space of plankton directly and then even affects the development of the whole aquatic ecosystem. As the spatial and temporal distribution/self-organization of phytoplankton is quite visible, it can reflect the "structure" of the aquatic ecosystem, which also reveals the strategy that phytoplankton takes to adapt to environmental changes. Therefore, investigation on the self-organization of phytoplankton has been essential to the understanding of ecosystem evolution and remains a hot topic in ecosystem dynamics and complexity.

One of the most striking manifestations of biological ocean dynamics is the proliferation of particularly dense phytoplankton, which often forms marvelous patterns with unexpectedly clear boundaries, such as banded patterns, chaotic patterns, and solitons. [2–4]. These patterns are usually produced by the interaction between the behavior of organisms (sinking, floating, or swimming) and the surrounding physical flow [3]. By examining the structure of dense phytoplankton mass reproduction, the local physical dynamics of living organisms, as well as behavioral and physiological responses, can be obtained. Patterns of some accumulations are the reflection of specific flows; observation of these visible patterns may reveal underlying dynamics [3]. However, the formation mechanism of these patterns is still unclear, and further research is urgently needed.

Since the environmental factors in the phytoplankton ecosystem vary with time, simple statistical models cannot accurately describe the dynamic process of phytoplankton growth in time and space. Therefore, the establishment of a dynamic model of plankton populations is an important method to study the physical and biological processes of plankton [5–10]. In 1949, Riley et al. established a vertical one-dimensional ecological dynamics model to simulate the seasonal changes of plankton in the North Sea of Europe, which symbolizes the study of aquatic ecosystems from qualitative description to the era of quantitative simulation [11]. In the same year, Monod, the founder of modern cell growth, proposed the famous Monod kinetic model, which describes the effect of substrate concentration on the cell growth rate, laying the foundation for the development of cell growth dynamics, thus promoting the development of phytoplankton growth dynamics [12]. After the Monod model was proposed, it was widely used in the study of phytoplankton growth dynamics [13–19] and found that the

Monod model is very suitable under certain conditions. Ye et al. used the Monod model to quantitatively study the relationship between phytoplankton biomass and nutrients in Taihu Lake [20]. It was found that total nitrogen is a key factor affecting the growth of phytoplankton, and eutrophication of lakes to phytoplankton growth has served as positive feedback. However, some studies have shown that the relationship between phytoplankton growth and nutrients does not follow the Monod model, which means that the Monod model has limitations [21]. Dugdale used the Michaelis–Menten model to describe the absorption of nutrients by planktonic algae under steady-state conditions [22, 23], revealing the effects of limited nutrient salts on the growth of planktonic algae. Studies have shown that it is feasible to describe the quantitative relationship between phytoplankton growth rate and nutrient salt concentration with Michaelis–Menten model under steady-state conditions [24].

Reaction-diffusion equations have been widely used to describe temporal and spatial complexity in ecology [25–33]. Time delay always exists and plays an important role in dynamical systems, and some dynamical phenomena could be affected by the time delay [34–37]. Turing bifurcation helps with the explanation of self-organization. Usually, Turing analysis is carried out on the basis of continuous models. In ecosystems, discrete models can generate more dynamical behaviors, which undoubtedly reflect ecological complexity [38, 39]. It is worth noting that numerical simulation is actually based on discrete forms of continuous systems, which automatically give numerical simulation algorithms. Therefore, the discrete form is the natural link between the actual model and the simulation. At the same time, in many cases, the environment exhibits considerable spatial variability and is best considered using spatial discrete methods [40–43]. Wang et al. studying the discrete forms of the Gierer–Meinhardt system found that discrete systems lead to more complex nonlinear behaviors and new dynamic phenomena than continuous forms. In addition, for the discrete time and space G-M system, they found a new instability mechanism, pronunciation flip-Turing instability [44]. In addition, when we apply Turing analysis on discrete models, there are some differences. First, the solution space of the continuous Turing model is infinite dimension, while the corresponding discretization model is in finite dimension. Secondly, in the linearization analysis of Turing bifurcation, elliptic operators have infinite eigenvalues and eigenvalue sequences are unbounded, while discrete elliptic operators have only finite eigenvalues. Therefore, it is of great significance to further reveal the formation mechanism of space-time self-organization by discretizing the reaction-diffusion equation in space and time. In this research, we use the N-S bifurcation theorem described by Guckenheimer and Holmes [45] to determine the conditions under which bifurcation occurs.

Therefore, in this research, we will investigate the self-organization of phytoplankton in a spatiotemporal discrete nutrient-phytoplankton model with time delay. The model is obtained through the discretization of a continuous nutrient-phytoplankton model proposed by Dai et al. [46]. Based on the discrete model, Neimark–Sacker bifurcation analysis and Turing bifurcation analysis are carried out, and parameter space is obtained correspondingly. Numerical simulations are then carried out using MATLAB (2011a) on the formation of phytoplankton patterns with different parameter values. Considering the pattern types and holistic shapes, the simulated phytoplankton patterns are compared with those observed in the real world. In addition, we also illustrate the results that can be obtained by the discrete model in the research are far more than those by the continuous model in [46].

2. Model and Analysis

2.1. A Discrete Spatiotemporal Nutrient-Phytoplankton Model with Delay. Considering the rate of diffusion of nutrients and phytoplankton is different in real-world systems, therefore, in this paper, we obtain the following spatial nutrient-phytoplankton models based on Ref. [46]:

$$\begin{cases} \dfrac{\partial N}{\partial t} = d_1 \Delta N + I - \dfrac{bN}{a+N} P - qN + \varepsilon m P, \\ \dfrac{\partial P}{\partial t} = d_2 \Delta P + \dfrac{\alpha b N \tau}{a + N\tau} P - mP, \end{cases} \tag{1}$$

where N and P represent nutrient concentration and the population biomass of phytoplankton, respectively. All parameters are non-negative and $N_\tau = N(x, t-\tau)$. Let $f_1(N,P) = I - (bN/(a+N))P - qN + \varepsilon mP$ and $g_1(N,P) = (\alpha b N\tau/(a+N\tau))P - mP$.

In the Turing instability analysis, people often give theoretical analysis to the continuous model, while the Turing pattern simulation undoubtedly adopts the corresponding discretization model. It is important to discretize the reaction-diffusion equation in space-time, which is of great significance for further revealing the formation mechanism of space-time self-organized structure. Therefore, in this paper, we consider the model on a $n \times n$ lattice, and the two variables can be expressed as $N^t_{i,j}$ and $P^t_{i,j}$ ($i, j \in \{1, 2, 3, \ldots, n\}$ and $t \in Z^+$), which represent the nutrient concentration and the phytoplankton density in lattice (i, j) at time t, respectively. According to the former research works of [39, 47], there are two stages, reaction stage and diffusion stage, when we discretize the continuous model (equation (1)). Meanwhile, we use a standard second-order central finite difference scheme to discretize (1) in space. The spatial dispersal stage, that is, diffusion, is considered firstly as

$$\begin{cases} N'_{(i,j,t)} = N^t_{i,j} + D_1 \nabla^2_d N^t_{i,j}, \\ P'_{(i,j,t)} = P^t_{i,j} + D_2 \nabla^2_d P^t_{i,j}, \end{cases} \tag{2}$$

where $D_1 = d_1 e/h^2$, $D_2 = d_2 e/h^2$, e, and h are the time interval and space interval. ∇^2_d denotes the discrete form of the Laplacian operator:

$$\begin{aligned} \nabla^2_d N^t_{i,j} &= N^t_{i+1,j} + N^t_{i-1,j} + N^t_{i,j+1} + N^t_{i,j-1} - 4N^t_{i,j}, \\ \nabla^2_d P^t_{i,j} &= P^t_{i+1,j} + P^t_{i-1,j} + P^t_{i,j+1} + P^t_{i,j-1} - 4P^t_{i,j}. \end{aligned} \tag{3}$$

Then, we consider the reaction stage:

$$\begin{cases} N_{i,j}^{t+1} = f\left(N'_{(i,j,t)}, P'_{(i,j,t)}\right) = N'_{(i,j,t)} + ef_1\left(N_{i,j}^t, P_{i,j}^t\right), \\ P_{i,j}^{t+1} = g\left(N'_{(i,j,t)}, P'_{(i,j,t)}\right) = P'_{(i,j,t)} + eg_1\left(N_{i,j}^t, P_{i,j}^t\right). \end{cases} \tag{4}$$

Boundary conditions are set as periodic conditions as follows:

$$\begin{cases} N_{i,0}^t = N_{i,k}^t, \\ N_{i,1}^t = N_{i,k+1}^t, \\ N_{0,j}^t = N_{k,j}^t, \\ N_{1,j}^t = N_{k+1,j}^t, \\ i, j \in (1, 2, \ldots, k), t \in Z^+. \end{cases} \tag{5}$$

Equations (2) and (4) including both diffusion and reaction stages are defined as our discrete model. According to the spatial homogeneity of the discrete system, with all i, j, and t, we have

$$\begin{aligned} \nabla_d^2 N_{i,j}^t &= 0, \\ \nabla_d^2 P_{i,j}^t &= 0. \end{aligned} \tag{6}$$

From (6), together with (2)–(4), then the homogeneous dynamics satisfies the following equation:

$$\begin{cases} N_{i,j}^{t+1} = N_{i,j}^t + e\left(I - \dfrac{bN_{i,j}^t}{a + N_{i,j}^t} P_{i,j}^t - qN_{i,j}^t + \varepsilon m P_{i,j}^t\right), \\ P_{i,j}^{t+1} = P_{i,j}^t + e\left(\dfrac{\alpha b N_{\tau_{i,j}^t}}{a + N_{\tau_{i,j}^t}} P_{i,j}^t - mP_{i,j}^t\right), \end{cases} \tag{7}$$

where $N\tau_{i,j}^t = N(i, j, t - \tau)$, we rewrite equation (7) into the form of maps:

$$\begin{pmatrix} N \\ P \end{pmatrix} \longrightarrow \begin{pmatrix} N + e\left(I - \dfrac{bN}{a+N} P - qN + \varepsilon m P\right) \\ P + e\left(\dfrac{\alpha b N_\tau}{a + N_\tau} P - mP\right) \end{pmatrix}. \tag{8}$$

In the sequel, we use (8) to analyze the homogeneous dynamics of equations (2)–(4).

2.2. Analysis of the Stability of the Homogeneous Steady State. The fixed point of map (8) is a homogeneous steady state of equations (2)–(4). So, we carry out the analysis of the stability about the fixed point of map (8). When both the delay and the diffusion are not considered, it is easy to see that map (8) has two fixed points: $E_0 = (I/q, 0)$ and $E^* = (N^*, P^*)$, where $P^* = \alpha(I\alpha b - \mathrm{Im} - qma)/m(1 - \varepsilon\alpha)(\alpha b - m)$ and $N^* = ma/(\alpha b - m)$. The sufficient and necessary conditions for that (N^*, P^*) is positive are as follows:

$$\begin{aligned} \alpha b - m &> 0, \\ I\alpha b - \mathrm{Im} - qma &> 0, \\ \varepsilon\alpha &< 1. \end{aligned} \tag{9}$$

The Jacobian matrix method is used to determine the local stability of fixed points. Since pattern formation requires the nontrivial homogeneous stationary state, which is corresponding to the fixed point (N^*, P^*), we just concern the stability of (N^*, P^*). The corresponding Jacobian is given by

$$J(e) = J\left(N^*, P^*\right) = \begin{pmatrix} 1 - e\left(q + \dfrac{(\alpha b - m)(\alpha bI - \mathrm{Im} - qma)}{abm\alpha(1 - \varepsilon\alpha)}\right) & e\left(\varepsilon m - \dfrac{m}{\alpha}\right) \\ e\dfrac{(\alpha b - m)(\alpha bI - \mathrm{Im} - qma)}{abm(1 - \varepsilon\alpha)} & 1 \end{pmatrix}. \tag{10}$$

The two eigenvalues of matrix (10) are as follows:

$$\lambda_{1,2} = \frac{tr(e) \pm \sqrt{tr(e)^2 - 4\Delta(e)}}{2}, \tag{11}$$

where

$$\begin{aligned} tr(e) &= 2 - \left(q + \frac{(\alpha b - m)(\alpha bI - \mathrm{Im} - qma)}{abm\alpha(1 - \varepsilon\alpha)}\right)e, \\ \Delta(e) &= 1 - \left(q + \frac{(\alpha b - m)(\alpha bI - \mathrm{Im} - qma)}{abm\alpha(1 - \varepsilon\alpha)}\right)e + \frac{(\alpha b - m)(\alpha bI - \mathrm{Im} - qma)}{\alpha ab}e^2. \end{aligned} \tag{12}$$

According to the criterion of stability of the fixed point, if $|\lambda_1| < 1$ and $|\lambda_2| < 1$, the fixed point is locally asymptotically stable. As shown in the previous research [48], this criterion of stability is equivalent to $\Delta(e) < 1$, $-(1 + \Delta(e)) < tr(e) < 1 + \Delta(e)$. Through calculations, the conditions for (N^*, P^*) to be locally asymptotically stable are determined as follows:

$$\begin{aligned} Ae^2 - Be &< 0, \\ A &> 0, \\ Ae^2 - 2Be + 4 &> 0, \end{aligned} \tag{13}$$

where

$$\begin{aligned} A &= \frac{(\alpha b - m)(\alpha bI - \mathrm{Im} - qma)}{\alpha ab}, \\ B &= q + \frac{(\alpha b - m)(\alpha bI - \mathrm{Im} - qma)}{abm\alpha(1 - \varepsilon\alpha)}. \end{aligned} \tag{14}$$

The dynamics of the discrete model without spatial diffusions can be shown in Figure 1, and the following bifurcations and simulations are all carried out in this situation. Note that, in the discrete system, the arrows in the figure represent the direction of iteration rather than dynamic flow. And $\tau = 0$ is considered, as when time delay increases, the following bifurcation will occur.

2.3. Bifurcation Analysis of the Homogeneous Steady State

2.3.1. Neimark–Sacker Bifurcation Analysis. In this part, we consider Neimark–Sacker bifurcation of equations (2)–(4) when τ is small. We first make a corresponding change to equation (1) and obtain equation (17) and then discretize equation (17) to obtain map (18).

If τ is small, $N_\tau = N(x,t) - \tau(\partial N(x,t)/\partial t)$, put it into equation (1) and obtain

$$\begin{cases} \dfrac{\partial N}{\partial t} = d_1 \Delta N + I - \dfrac{bN}{a+N} P - qN + \varepsilon mP, \\ \dfrac{\partial P}{\partial t} = d_2 \Delta P + \alpha bP\left(R\left(N(x,t) - \tau \dfrac{\partial N(x,t)}{\partial t}\right)\right) - mP, \end{cases} \tag{15}$$

in which

$$R(N) = \frac{N}{N+a}. \tag{16}$$

Taylor expansion of $R(N(x,t) - \tau(\partial N(x,t)/\partial t))$ at (N, P) without considering the higher order nonlinear part and equation (1) can be written as

$$\begin{cases} \dfrac{\partial N(x,t)}{\partial t} = d_1 \Delta N + f_1(N,P), \\ \dfrac{\partial P(x,t)}{\partial t} = -\dfrac{\alpha abP\tau}{(N+a)^2} d_1 \Delta N + d_2 \Delta P + g_2(N,P) - \dfrac{\alpha abP\tau}{(N+a)^2} f_1(N,P), \end{cases} \tag{17}$$

where $f_1(N,P) = I - (bN/(a+N))P - qN + \varepsilon mP$ and $g_2(N,P) = (\alpha bN/(a+N))P - mP$. Therefore, equation (8) can be expressed as the following map:

$$\begin{pmatrix} N \\ P \end{pmatrix} \longrightarrow \begin{pmatrix} N + eI - \dfrac{ebN}{N+a} P - eqN + e\varepsilon mP \\ P + e\dfrac{\alpha bNP}{a+N} - emP - \dfrac{\alpha abP\tau}{(N+a)^2} e\left(I - \dfrac{bN}{N+a} P - qN + \varepsilon mP\right) \end{pmatrix}. \tag{18}$$

According to [48], the first condition of Neimark–Sacker bifurcation requires the eigenvalues at a fixed point, λ_1 and λ_2 are conjugate and their modules are 1, shown as

$$\begin{aligned} \lambda_2 &= \overline{\lambda_1}, \\ |\lambda_1| &= |\lambda_2| = 1, \end{aligned} \tag{19}$$

in which

$$\lambda_{1,2} = \frac{tr_0 \pm \sqrt{tr_0^2 - 4\Delta_0}}{2}, \tag{20}$$

$$\begin{aligned} tr_0 &= a_{11} + a_{22} = A_0 + A_1 + A_2\tau, \\ \Delta_0 &= a_{11}a_{22} - a_{12}a_{21} = A_0(A_1 + A_2\tau) - B_0(B_1 + B_2\tau), \end{aligned} \tag{21}$$

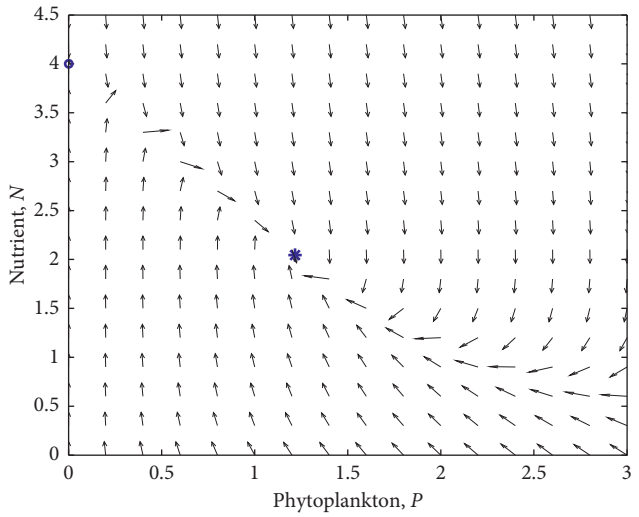

Figure 1: Fixed points of (8). Parameter values: $I = 1.6$, $a = 0.5$, $b = 0.8$, $\alpha = 0.7$, $m = 0.45$, $q = 0.01$, $\varepsilon = 0.001$, and $\tau = 0$. *Asymptotically stable fixed point E^*; "○" represents the boundary fixed point E_0.

$A_0, A_1, A_2, B_0, B_1, B_2, a_{11}, a_{12}, a_{21}$, and a_{22} have been shown in Appendix A.

Then, we can get

$$tr_0^2 - 4\Delta_0 < 0, \quad \Delta_0 = 1. \tag{22}$$

By calculation, we can obtain the Neimark–Sacker bifurcation point τ_0:

$$\tau_0 = \frac{1 + B_0B_1 - A_0A_1}{A_0A_2 - B_0B_2}. \tag{23}$$

Under the satisfaction of conditions (22) and (23), the fixed point E^* of map (18) is translated to the origin by the following translation:

$$\begin{aligned} x &= N - N^*, \\ y &= P - P^*. \end{aligned} \tag{24}$$

Then, map (18) is transformed into

$$\begin{pmatrix} x \\ y \end{pmatrix} \longrightarrow \begin{pmatrix} a_{11}x + a_{12}y + a_{13}x^2 + a_{14}y^2 + a_{15}xy + a_{16}x^3 + a_{17}x^2y + a_{18}xy^2 + O\left((|x| + |y|)^4\right) \\ a_{21}x + a_{22}y + a_{23}x^2 + a_{24}y^2 + a_{25}xy + a_{26}x^3 + a_{27}x^2y + a_{28}xy^2 + O\left((|x| + |y|)^4\right) \end{pmatrix}, \tag{25}$$

where $a_{11}, a_{12}, a_{13}, a_{14}, a_{15}, a_{16}, a_{17}, a_{18}, a_{21}, a_{22}, a_{23}, a_{24}, a_{25}, a_{26}, a_{27}$, and a_{28} have been shown in Appendix A with $\tau = \tau_0$.

The second condition for Neimark–Sacker bifurcation requires

$$d = \left.\frac{\mathrm{d}|\lambda(\tau)|}{\mathrm{d}\tau}\right|_{\tau=\tau_0} = \frac{A_0A_2 - B_0B_2}{2\sqrt{A_0A_1 - B_0B_1 + (A_0A_2 - B_0B_2)\tau_0}} \neq 0,$$

$$(\lambda(\tau_0))^\theta \neq 1, \quad \theta = 1, 2, 3, 4, \tag{26}$$

in which

$$\lambda(\tau_0),$$

$$\overline{\lambda}(\tau_0) = \frac{tr_0(\tau_0)}{2} \pm \frac{i}{2}\sqrt{4\Delta_0(\tau_0) - tr_0^2(\tau_0)} = \beta \pm i\gamma, \tag{27}$$

$$i = \sqrt{-1},$$

where $tr_0(\tau_0)$ and $\Delta_0(\tau_0)$ are described in equation (21) with $\tau = \tau_0$. Then, we can obtain

$$A_0 + A_1 + A_2\tau_0 \neq 0, -1. \tag{28}$$

On the basis of map (25), the canonical form is studied to obtain the last condition for the occurrence of Neimark–Sacker bifurcation. The invertible transformation is applied:

$$\begin{pmatrix} x \\ y \end{pmatrix} = \begin{pmatrix} a_{12} & 0 \\ \beta - a_{11} & -\gamma \end{pmatrix} \begin{pmatrix} \tilde{x} \\ \tilde{y} \end{pmatrix}. \tag{29}$$

To map (25), then the map becomes

$$\begin{pmatrix} \tilde{x} \\ \tilde{y} \end{pmatrix} \longrightarrow \begin{pmatrix} \beta & -\gamma \\ \gamma & \beta \end{pmatrix} \begin{pmatrix} \tilde{x} \\ \tilde{y} \end{pmatrix} + \frac{1}{a_{12}\gamma} \begin{pmatrix} F(\tilde{x}, \tilde{y}) \\ G(\tilde{x}, \tilde{y}) \end{pmatrix}, \tag{30}$$

where

$$\begin{aligned} F(\tilde{x}, \tilde{y}) &= a_{12}\gamma(a_{12}a_{13} + a_{15}(\beta - a_{11}))\tilde{x}^2 - a_{12}a_{15}\gamma^2\tilde{x}\tilde{y} \\ &\quad + a_{12}^2\gamma(a_{12}a_{16} + a_{17}(\beta - a_{11}))\tilde{x}^3 - a_{12}^2a_{17}\gamma^2\tilde{x}^2\tilde{y} \\ &\quad + O\left((|\tilde{x}| + |\tilde{y}|)^4\right), \\ G(\tilde{x}, \tilde{y}) &= \left(a_{12}^2(a_{13}(\beta - a_{11}) - a_{12}a_{23}) + (a_{14}(\beta - a_{11}) \right. \\ &\quad \left. - a_{12}a_{24})(\beta - a_{11})^2 + \left(a_{12}a_{15}(\beta - a_{11}) - a_{12}^2a_{25}\right) \right. \\ &\quad \left. \cdot (\beta - a_{11})\right)\tilde{x}^2 - a_{12}a_{24}\gamma^2\tilde{y}^2 + a_{12}\gamma((2a_{24} - a_{15}) \right. \\ &\quad \left. \cdot (\beta - a_{11}) + a_{12}a_{25})\tilde{x}\tilde{y} + \left(\left(a_{12}^3a_{16}(\beta - a_{11}) - a_{12}^4a_{26}\right) \right. \\ &\quad \left. + \left(a_{12}^2a_{17}(\beta - a_{11}) - a_{12}^3a_{27}\right)(\beta - a_{11}) - a_{12}^2a_{28} \right. \\ &\quad \left. \cdot \left(\beta - a_{11}^2\right)\right)\tilde{x}^3 - a_{12}^2\gamma((a_{17}(\beta - a_{11}) - a_{12}a_{27}) \right. \\ &\quad \left. - 2a_{28}(\beta - a_{11}))\tilde{x}^2\tilde{y} - a_{12}^2a_{28}\gamma^2\tilde{x}\tilde{y}^2 + O\left((|\tilde{x}| + |\tilde{y}|)^4\right). \end{aligned} \tag{31}$$

The second-order and third-order partial derivatives of $F(\widetilde{x},\widetilde{y})$ and $G(\widetilde{x},\widetilde{y})$ at $(0,0)$ are calculated as

$$\begin{aligned}
F_{\widetilde{x}\widetilde{x}} &= 2a_{12}^2a_{13}\gamma + 2a_{12}a_{15}\gamma(\beta - a_{11}),\\
F_{\widetilde{x}\widetilde{y}} &= -a_{12}a_{15}\gamma^2,\\
F_{\widetilde{y}\widetilde{y}} &= 0,\\
F_{\widetilde{x}\widetilde{x}\widetilde{x}} &= 6a_{12}^3a_{16}\gamma + 6a_{12}^2a_{17}\gamma(\beta - a_{11}),\\
F_{\widetilde{x}\widetilde{x}\widetilde{y}} &= -a_{12}^2a_{17}\gamma^2,\\
F_{\widetilde{x}\widetilde{y}\widetilde{y}} &= 0,\\
F_{\widetilde{y}\widetilde{y}\widetilde{y}} &= 0,\\
G_{\widetilde{x}\widetilde{x}} &= 2a_{12}^2(a_{13}(\beta - a_{11}) - a_{12}a_{23})\\
&\quad + 2(a_{14}(\beta - a_{11}) - a_{12}a_{24})(\beta - a_{11})^2\\
&\quad + 2(\beta - a_{11})\left(a_{12}a_{15}(\beta - a_{11}) - a_{12}^2a_{25}\right),\\
G_{\widetilde{x}\widetilde{y}} &= 2\gamma a_{12}a_{24}(\beta - a_{11}) - \gamma\left(a_{12}a_{15}(\beta - a_{11}) - a_{12}^2a_{25}\right),\\
G_{\widetilde{y}\widetilde{y}} &= -2a_{12}a_{24}\gamma^2,\\
G_{\widetilde{x}\widetilde{x}\widetilde{x}} &= 6\left(a_{12}^3a_{16}(\beta - a_{11}) - a_{12}^4a_{26}\right)\\
&\quad + 6\left(a_{12}^2a_{17}(\beta - a_{11}) - a_{12}^3a_{27}\right)(\beta - a_{11})\\
&\quad - 6a_{12}^2a_{28}(\beta - a_{11})^2,\\
G_{\widetilde{x}\widetilde{x}\widetilde{y}} &= -2\gamma\left(a_{12}^2a_{17}(\beta - a_{11}) - a_{12}^3a_{27}\right) + 4\gamma a_{12}^2a_{28}(\beta - a_{11}),\\
G_{\widetilde{x}\widetilde{y}\widetilde{y}} &= -2a_{12}^2a_{28}\gamma^2,\\
G_{\widetilde{y}\widetilde{y}\widetilde{y}} &= 0.
\end{aligned} \tag{32}$$

The third condition of Neimark–Sacker bifurcation requires

$$R = -\mathrm{Re}\left(\frac{(1-2\overline{\lambda})\overline{\lambda}^2}{1-\lambda}\xi_{11}\xi_{20}\right) - \frac{1}{2}|\xi_{11}|^2 - |\xi_{02}|^2 + \mathrm{Re}\left(\overline{\lambda}\xi_{21}\right) \neq 0, \tag{33}$$

in which

$$\begin{aligned}
\xi_{11} &= \frac{1}{4a_{12}\gamma}\left(\left(F_{\widetilde{x}\widetilde{x}} + F_{\widetilde{y}\widetilde{y}}\right) + i\left(G_{\widetilde{x}\widetilde{x}} + G_{\widetilde{y}\widetilde{y}}\right)\right),\\
\xi_{20} &= \frac{1}{8a_{12}\gamma}\left(\left(F_{\widetilde{x}\widetilde{x}} - F_{\widetilde{y}\widetilde{y}} + 2G_{\widetilde{x}\widetilde{y}}\right) + i\left(G_{\widetilde{x}\widetilde{x}} - G_{\widetilde{y}\widetilde{y}} - 2F_{\widetilde{x}\widetilde{y}}\right)\right),\\
\xi_{02} &= \frac{1}{8a_{12}\gamma}\left(\left(F_{\widetilde{x}\widetilde{x}} - F_{\widetilde{y}\widetilde{y}} - 2G_{\widetilde{x}\widetilde{y}}\right) + i\left(G_{\widetilde{x}\widetilde{x}} - G_{\widetilde{y}\widetilde{y}} + 2F_{\widetilde{x}\widetilde{y}}\right)\right),\\
\xi_{21} &= \frac{1}{16a_{12}\gamma}\left(\left(F_{\widetilde{x}\widetilde{x}\widetilde{x}} + F_{\widetilde{x}\widetilde{y}\widetilde{y}} + G_{\widetilde{x}\widetilde{x}\widetilde{y}} + G_{\widetilde{y}\widetilde{y}\widetilde{y}}\right)\right.\\
&\quad \left. + i\left(G_{\widetilde{x}\widetilde{x}\widetilde{x}} + G_{\widetilde{x}\widetilde{y}\widetilde{y}} - F_{\widetilde{x}\widetilde{x}\widetilde{y}} - F_{\widetilde{y}\widetilde{y}\widetilde{y}}\right)\right).
\end{aligned} \tag{34}$$

After calculation, the third condition for Neimark–Sacker can be expressed as

$$\begin{aligned}
R = -\frac{1}{A^*}&\left\{B^*\left[\left(F_{\widetilde{x}\widetilde{x}} + F_{\widetilde{y}\widetilde{y}}\right)\left(F_{\widetilde{x}\widetilde{x}} - F_{\widetilde{y}\widetilde{y}} + 2G_{\widetilde{x}\widetilde{y}}\right)\right.\right.\\
&\left. - \left(G_{\widetilde{x}\widetilde{x}} + G_{\widetilde{y}\widetilde{y}}\right)\left(G_{\widetilde{x}\widetilde{x}} - G_{\widetilde{y}\widetilde{y}} - 2F_{\widetilde{x}\widetilde{y}}\right)\right]\\
&+ C^*\left[\left(G_{\widetilde{x}\widetilde{x}} + G_{\widetilde{y}\widetilde{y}}\right)\left(F_{\widetilde{x}\widetilde{x}} - F_{\widetilde{y}\widetilde{y}} + 2G_{\widetilde{x}\widetilde{y}}\right)\right.\\
&\left.\left. - \left(F_{\widetilde{x}\widetilde{x}} + F_{\widetilde{y}\widetilde{y}}\right)\left(G_{\widetilde{x}\widetilde{x}} - G_{\widetilde{y}\widetilde{y}} - 2F_{\widetilde{x}\widetilde{y}}\right)\right]\right\}\\
&- \frac{1}{32a_{12}^2\gamma^2}\left[\left(F_{\widetilde{x}\widetilde{x}} + F_{\widetilde{y}\widetilde{y}}\right)^2 + \left(G_{\widetilde{x}\widetilde{x}} + G_{\widetilde{y}\widetilde{y}}\right)^2\right]\\
&+ \frac{1}{16a_{12}\gamma}\left[\beta\left(F_{\widetilde{x}\widetilde{x}\widetilde{x}} + F_{\widetilde{x}\widetilde{y}\widetilde{y}} + G_{\widetilde{x}\widetilde{x}\widetilde{y}} + G_{\widetilde{y}\widetilde{y}\widetilde{y}}\right)\right.\\
&\left. + \gamma\left(G_{\widetilde{x}\widetilde{x}\widetilde{x}} + G_{\widetilde{x}\widetilde{y}\widetilde{y}} - F_{\widetilde{x}\widetilde{x}\widetilde{y}} - F_{\widetilde{y}\widetilde{y}\widetilde{y}}\right)\right]\\
&- \frac{1}{64a_{12}^2\gamma^2}\left[\left(F_{\widetilde{x}\widetilde{x}} - F_{\widetilde{y}\widetilde{y}} - 2G_{\widetilde{x}\widetilde{y}}\right)^2\right.\\
&\left. + \left(G_{\widetilde{x}\widetilde{x}} - G_{\widetilde{y}\widetilde{y}} + 2F_{\widetilde{x}\widetilde{y}}\right)^2\right] \neq 0,
\end{aligned} \tag{35}$$

in which

$$\begin{aligned}
A^* &= 32a_{12}^2\gamma^2\left((1-\beta) + \gamma^2\right),\\
B^* &= \left(1 - 3\beta + 2\beta^2 - 2\gamma^2\right)\left(\beta^2 - \gamma^2\right) + \left(6\beta - 8\beta^2\right)\gamma^2,\\
C^* &= 2\beta\gamma\left((1-\beta)(1-2\beta) - 2\gamma^2\right) - \gamma(3 - 4\beta)\left(\beta^2 - \gamma^2\right).
\end{aligned} \tag{36}$$

Based on the above calculations, when the conditions (23), (28), and (35) are satisfied, Neimark–Sacker bifurcation occurs at the fixed point E^*. Moreover, when $R < 0$ and $d > 0$, then an attracting invariant closed curve bifurcates from the fixed point E^* for $\tau > \tau_0$; otherwise, when $R > 0$ and $d > 0$, a repelling invariant closed curve bifurcates from the fixed point E^* for $0 < \tau < \tau_0$.

In Figure 2(a), the parameter space of time delay and input rate $I - \tau$ is shown. Zone I represents that when the input rate of nutrient is low, positive fixed point E^* does not exist. Zone II and III represent no bifurcation and bifurcation area around the fixed point E^*. And Figure 2(b) shows the bifurcation diagram when $I = 1.6$ and $e = 0.2$. The Hopf bifurcation point is not suitable here with a time step e not small enough, while the calculated Neimark–Sacker bifurcation point is more correct compared with the simulated bifurcation point. This difference can be shown in Figure 2(d): e cannot be equal to 0.2, but in the discrete model, when $e = 0.2$, Neimark–Sacker bifurcation occurs and drives the system from stable fixed point to quasiperiodic dynamics. When time delay $\tau = 3$ satisfy both $\tau > \tau_{N-S}$ and $\tau > \tau_{\mathrm{Hopf}}$, the dynamics of the continuous model (with $e = 0.01$ as in [46]) and the discrete model ($e = 0.2$) show

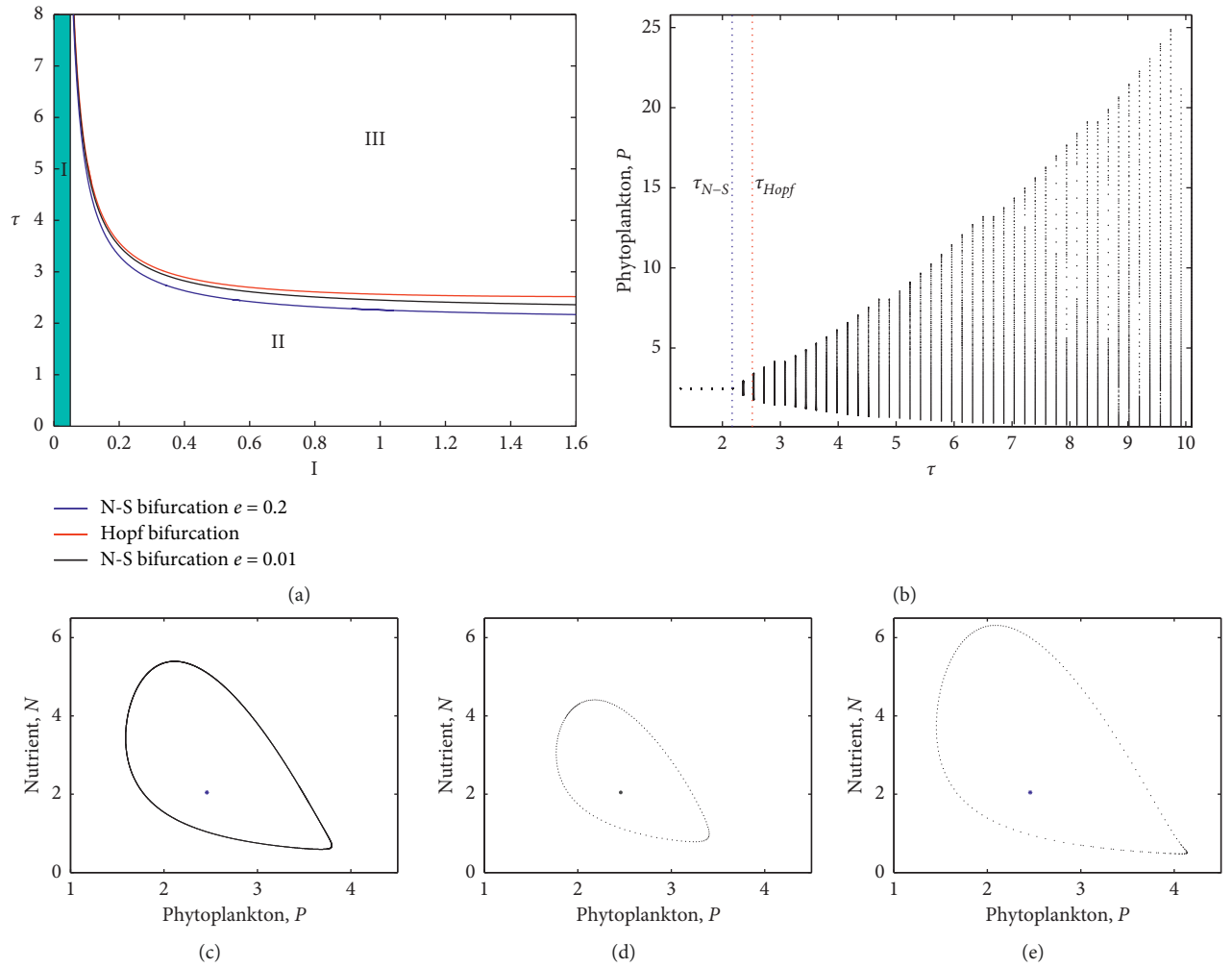

FIGURE 2: (a) Parameter space graph of Neimark–Sacker bifurcation and Hopf bifurcation with I and τ; (b) bifurcation diagram of Neimark–Sacker bifurcation with τ and phytoplankton; (c–e) phase portraits of Neimark–Sacker bifurcation with parameters (c) $e = 0.01$, $\tau = 3$; (d) $e = 0.2$, $\tau = 2.45$; (e) $e = 0.2$, $\tau = 3$. Other parameter values: $I = 1.6$, $a = 0.5$, $b = 0.8$, $\alpha = 0.7$, $m = 0.45$, $q = 0.01$, and $\varepsilon = 0.001$. *Asymptotically stable fixed point E^*.

differences: Hopf bifurcation induces the continuous system into a limit cycle (Figure 2(c)); Neimark–Sacker bifurcation induces the discrete system into quasiperiodic iteration and the amplitude of variables is larger.

2.3.2. Turing Bifurcation Analysis. In this part, we consider Turing bifurcation of equations (2)–(4) when $\tau = 0$. Turing bifurcation requires two conditions. Firstly, a nontrivial homogeneous stationary state exists and is stable to spatially homogeneous perturbations, which has been obtained in the above section. Secondly, the stable stationary state is unstable to at least one type of spatially heterogeneous perturbations. This paper is based on the method of Bai and Zhang to do Turing bifurcation analysis of the discrete model [49]. We first consider the following eigenvalue equation:

$$\nabla^2 X^{ij} + \lambda X^{ij} = 0, \tag{37}$$

with periodic boundary conditions:

$$\begin{aligned} X^{i,0} &= X^{i,k}, \\ X^{i,1} &= X^{i,k+1}, \\ X^{0,j} &= X^{k,j}, \\ X^{1,j} &= X^{k+1,j}, \\ i, j &\in (1, 2, \ldots, k). \end{aligned} \tag{38}$$

When $x \neq 0$ and $y \neq 0$, we set $X^{ij} = x^i y^j$, put it into equation (38), and obtain $x^k = y^k = 1$. Then, we can get

$$\begin{aligned} x_r &= \exp\left(\frac{2(r-1)\pi}{k} i'\right), \\ y_l &= \exp\left(\frac{2(l-1)\pi}{k} i'\right), \\ r, l &\in (1, 2, \ldots, k), i' = \sqrt{-1}. \end{aligned} \tag{39}$$

Substituting $X^{ij} = x^i y^j$ into equation (37), we obtain that

$$x^{i-1}y^j + x^{i+1}y^j + x^i y^{j-1} + x^i y^{j+1} - 4x^i y^j + \lambda x^i y^j = 0. \tag{40}$$

By calculating $\lambda = -((1-x)^2/x) - ((1-y)^2/y)$, then, using equation (39) we can get

$$\begin{aligned}\lambda_{rl} &= -\frac{(1-x_r)^2}{x_r} - \frac{(1-y_l)^2}{y_l} \\ &= 4\left(\sin^2\frac{(r-1)\pi}{k} + \sin^2\frac{(l-1)\pi}{k}\right) = S_{rl}^2.\end{aligned} \tag{41}$$

Turing bifurcation is caused by the lack of spatial symmetry. To analyze the Turing bifurcation, a spatially nonuniform perturbation is applied at the spatially uniform state E^*. The equation for spatially nonuniform perturbations can be expressed as

$$\begin{aligned}\widetilde{N}_{i,j}^t &= N_{i,j}^t - N^*, \\ \widetilde{P}_{i,j}^t &= P_{i,j}^t - P^*.\end{aligned} \tag{42}$$

Noticing $\nabla_d^2 \widetilde{N}_{i,j}^t = \nabla_d^2 N_{i,j}^t$ and $\nabla_d^2 \widetilde{P}_{i,j}^t = \nabla_d^2 P_{i,j}^t$, and the values of the two cannot be constant to 0. Substituting equation (42) into equations (2)–(4) leads to the following equation:

$$\begin{cases}\widetilde{N}_{i,j}^{t+1} = f_N\left(\widetilde{N}_{i,j}^t + D_1\nabla_d^2\widetilde{N}_{i,j}^t\right) + f_P\left(\widetilde{P}_{i,j}^t + D_2\nabla_d^2\widetilde{P}_{i,j}^t\right) + O\left(\left(\left|\widetilde{N}_{i,j}^t\right| + \left|\widetilde{P}_{i,j}^t\right|\right)^2\right), \\ \widetilde{P}_{i,j}^{t+1} = g_N\left(\widetilde{N}_{i,j}^t + D_1\nabla_d^2\widetilde{N}_{i,j}^t\right) + g_P\left(\widetilde{P}_{i,j}^t + D_2\nabla_d^2\widetilde{P}_{i,j}^t\right) + O\left(\left(\left|\widetilde{N}_{i,j}^t\right| + \left|\widetilde{P}_{i,j}^t\right|\right)^2\right).\end{cases} \tag{43}$$

The high-order terms in the above equations can be ignored when the disturbance is very weak. Using the corresponding characteristic function X_{rl}^{ij} of the eigenvalue λ_{rl} to multiply equation (43), we obtain

$$\begin{cases}X_{rl}^{ij}\widetilde{N}_{i,j}^{t+1} = f_N X_{rl}^{ij}\widetilde{N}_{i,j}^t + f_P X_{rl}^{ij}\widetilde{P}_{i,j}^t + D_1 f_N X_{rl}^{ij}\nabla_d^2\widetilde{N}_{i,j}^t + D_2 f_P X_{rl}^{ij}\nabla_d^2\widetilde{P}_{i,j}^t, \\ X_{rl}^{ij}\widetilde{P}_{i,j}^{t+1} = g_N X_{rl}^{ij}\widetilde{N}_{i,j}^t + g_P X_{rl}^{ij}\widetilde{P}_{i,j}^t + D_1 g_N X_{rl}^{ij}\nabla_d^2\widetilde{N}_{i,j}^t + D_2 g_P X_{rl}^{ij}\nabla_d^2\widetilde{P}_{i,j}^t.\end{cases} \tag{44}$$

Summing equation (44) for all i and j gives the following equation:

$$\begin{cases}\Sigma X_{rl}^{ij}\widetilde{N}_{i,j}^{t+1} = f_N\Sigma X_{rl}^{ij}\widetilde{N}_{i,j}^t + f_P\Sigma X_{rl}^{ij}\widetilde{P}_{i,j}^t + D_1 f_N\Sigma X_{rl}^{ij}\nabla_d^2\widetilde{N}_{i,j}^t + D_2 f_P\Sigma X_{rl}^{ij}\nabla_d^2\widetilde{P}_{i,j}^t, \\ \Sigma X_{rl}^{ij}\widetilde{P}_{i,j}^{t+1} = g_N\Sigma X_{rl}^{ij}\widetilde{N}_{i,j}^t + g_P\Sigma X_{rl}^{ij}\widetilde{P}_{i,j}^t + D_1 g_N\Sigma X_{rl}^{ij}\nabla_d^2\widetilde{N}_{i,j}^t + D_2 g_P\Sigma X_{rl}^{ij}\nabla_d^2\widetilde{P}_{i,j}^t.\end{cases} \tag{45}$$

Let $\overline{N}_t = \sum_{i,j=1}^k X_{rl}^{ij}\widetilde{N}_{ij}^{t+1}$ and $\overline{P}_t = \sum_{i,j=1}^k X_{rl}^{ij}P_{ij}^{t+1}$, combined boundary conditions (38), equation (45) can be transformed into the following form:

$$\begin{cases}\overline{N}_{t+1} = f_N(1 - D_1\lambda_{rl})\overline{N}_t + f_P(1 - D_2\lambda_{rl})\overline{P}_t, \\ \overline{P}_{t+1} = g_N(1 - D_1\lambda_{rl})\overline{N}_t + g_P(1 - D_2\lambda_{rl})\overline{P}_t.\end{cases} \tag{46}$$

At this time, we know that a progressive solution of equations (2)–(4) with boundary conditions (5) is $N_{ij}^t = \overline{N}_t X_{rl}^{ij}$ and $P_{ij}^t = \overline{P}_t X_{rl}^{ij}$. Therefore, we know that if the solution of the equation (46) is unstable, it will cause the equations (2)–(4) to be unstable. The eigenvalues of equations (2)–(4) are as follows:

$$\lambda_\pm(r,l,e) = \frac{1}{2}tr(r,l,e) \pm \frac{1}{2}\sqrt{tr(r,l,e)^2 - 4\Delta(r,l,e)}, \tag{47}$$

in which

$$tr(r,l,e) = a_{11}(e) + a_{22}(e) - \frac{e}{h^2}\left(a_{11}(e)d_1 + a_{22}(e)d_2\right)\lambda_{rl},$$

$$\Delta(r,l,e) = \left(a_{11}(e)a_{22}(e) - a_{12}(e)a_{21}(e)\right)\left(1 - \frac{e}{h^2}d_1\lambda_{rl}\right)\left(1 - \frac{e}{h^2}d_2\lambda_{rl}\right),$$

$$J(N^*, P^*) = \begin{vmatrix} a_{11}(e) & a_{12}(e) \\ a_{21}(e) & a_{22}(e) \end{vmatrix} = \begin{vmatrix} 1 - eq - \dfrac{eab}{(N^*+a)^2}P^* & e\varepsilon m - \dfrac{ebN^*}{N^*+a} \\ \dfrac{e\alpha ab}{(N^*+a)^2}P^* & 1 - em + \dfrac{e\alpha bN^*}{N^*+a} \end{vmatrix}. \tag{48}$$

Here, $a_{11}(e)$, $a_{12}(e)$, $a_{21}(e)$, and $a_{22}(e)$ are denoted for reminding that they are dependent on e. Based on the two eigenvalues, we define

$$\begin{cases} \lambda_m(r,l,e) = \max\left(\left|\lambda_+(r,l)\right|, \left|\lambda_-(r,l)\right|\right), \\ \lambda_m(e) = \max_{r=1,l=1}^{n}\lambda_m(r,l,e). \end{cases} \tag{49}$$

The occurrence of Turing bifurcation needs to satisfy $\lambda_m(e) = 1$. According to this condition, we can determine the critical value e' of Turing bifurcation occurring, which can be described as follows:

(1) If $tr(r,l,e)^2 > 4\Delta(r,l,e)$ is satisfied in a small neighborhood of $e = e'$, the critical value e' satisfies $\max_{r=1,l=1}^{n}(|tr(r,l,e')| - \Delta(r,l,e')) = 1$

(2) If $tr(r,l,e)^2 \le 4\Delta(r,l,e)$ is satisfied in a small neighborhood of $e = e'$, the critical value e' satisfies $\max_{r=1,l=1}^{n}\Delta(r,l,e') = 1$

$\max_{r=1,l=1}^{n}(|tr(r,l,e')| - \Delta(r,l,e')) = 1$ and $\max_{r=1,l=1}^{n}\Delta(r,l,e') = 1$ determine the critical conditions for the occurrence of Turing bifurcation in discrete systems. From this critical condition, the conditions for the formation of the Turing pattern can be obtained. By simplifying the two cases described above, it can be known that Turing instability occurs and leads to the formation of spatial heterogeneity patterns when $\lambda_m(e) > 1$.

Then, we discuss the influence of the diffusion coefficients d_1 and d_2 on the model. We use the following parameter values: $I = 1.6$, $a = 0.5$, $b = 0.8$, $\alpha = 0.7$, $q = 0.01$, $\varepsilon = 0.001$, $m = 0.45$, $d_1 = 0.2$, $d_2 = 0.2$, $e = 0.2$, $h = 1$, $\tau = 0$, and $t = 100$. The discrete model is solved numerically in a rectangular spatial grid consisting of 100×100 units, and periodic boundary conditions are adopted. As shown in Figure 3, Turing bifurcation can be displayed via the change of eigenvalue $\lambda(k,l)$. In Figure 3(a), we can see that the perturbation parameters k and l have symmetrical effects on the eigenvalues. Therefore, for convenience of observation, let $k = l$, then we can get the change in the eigenvalue to l, as shown in Figure 3(b). If there is no disturbance, the system will be at a stable point. But, when there is disturbance, Turing bifurcation can happen. According to Figure 3(b), we can know that if the diffusion coefficient $d_1 = 1.220$, then the eigenvalue of the system will not make the eigenvalue $\lambda(k,l)$ greater than 1 with the increase of the perturbation parameter; at this time, Turing bifurcation will not occur. When $d_1 = 1.389$, the curve is tangent to the straight line $\lambda(k,l) = 1$, that is, only if the diffusion coefficient $d_1 > 1.389$, the value of the eigenvalue $\lambda(k,l)$ will exceed 1 as the disturbance coefficient increases; at this time, Turing bifurcation will occur in the system.

3. Numerical Simulations

In this section, numerical simulations on the formation of phytoplankton are carried out focusing on three aspects including time delay τ and diffusion coefficients d_1 and d_2. Note that initial conditions are set as homogeneous steady states on 100×100 (mostly) lattice with ±5% random perturbations. Then simulated patterns are compared with real observed patterns.

3.1. Effects of Time Delay on the Pattern Formation. According to the stability analysis and Neimark–Sacker bifurcation analysis, time delay can cause the instability of the system. As shown in Figure 4, with given parameter values, the critical value of can be calculated as $\tau_0 \approx 2.2703$. Thus, we take $\tau = 0$, $\tau = 1$, and $\tau = 3$ and obtain Figures 4(a)–4(c) respectively. Figures 4(a) and 4(b) show that when $0 \le \tau < \tau_0$, there is no spatial patterns. Figure 4(c) clearly shows the formation of a Neimark–Sacker type pattern when $\tau > \tau_0$. From the simulated patterns, we can see that simulations are consistent with the Neimark–Sacker analysis.

Figure 5 shows a time series of phytoplankton pattern formation process from initial conditions to self-organization when $\tau = 3$. Small patches can be formed at the beginning (Figures 5(b) and 5(c)), and then gradually forming spirals (Figure 5(d)). The spirals will break with time, and reform afterwards (Figures 5(e)–5(g)). Then cloud-like patterns will finally be formed (Figures 5(h) and 5(i)).

3.2. Effects of Diffusion Coefficients on the Pattern Formation. Based on the Turing bifurcation analysis in Section 2.3.2, we can see that the diffusion coefficient d_1 can induce the occurrence of Turing bifurcations, and the critical value is $d_1 = 1.389$. Figure 6(a) shows that there is no pattern, while in Figure 6(b) we can clearly see the appearance of a typical banded Turing-type pattern. In addition, diffusion coefficient d_2 can also induce the occurrence of Turing bifurcation as shown in Figure 6(c). The simulations are quite consistent with the above analysis of Turing bifurcation.

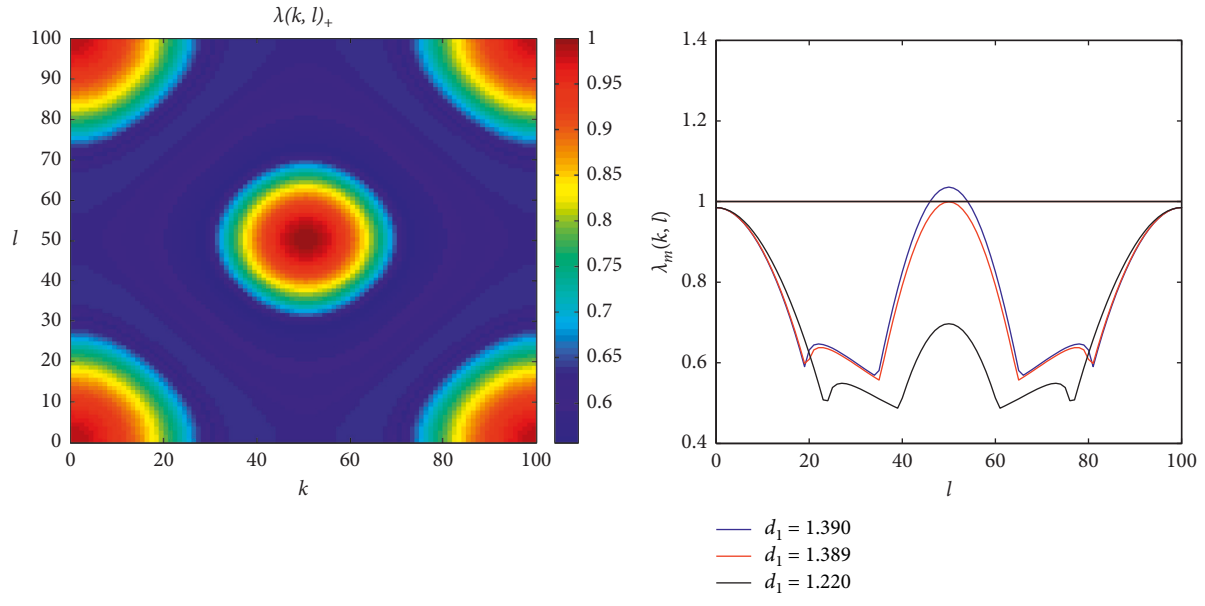

(a) (b)

Figure 3: Variation of eigenvalues $\lambda(k,l)$ with perturbation numbers k and l. Parameter values: $I = 1.6$, $a = 0.5$, $b = 0.8$, $\alpha = 0.7$, $e = 0.2$, $m = 0.45$, $d_2 = 0.20$, $q = 0.01$, $\tau = 0$, $h = 1$, $\varepsilon = 0.001$, and $n = 100$.

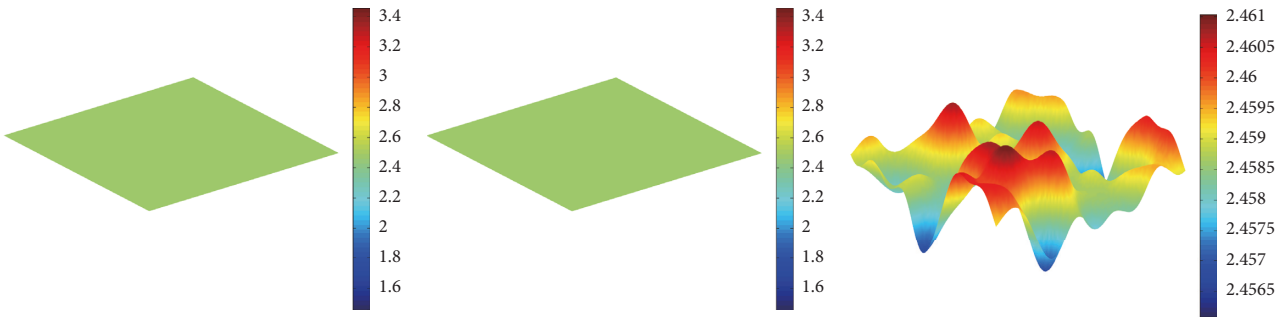

(a) (b) (c)

Figure 4: Spatial distribution of phytoplankton population under different time delay parameters. Parameter values: $I = 1.6$, $a = 0.5$, $b = 0.8$, $\alpha = 0.7$, $m = 0.45$, $d_1 = 0.20$, $d_2 = 0.20$, $q = 0.01$, $\varepsilon = 0.001$, and $t = 800$. (a) $\tau = 0$; (b) $\tau = 1$; (c) $\tau = 3$.

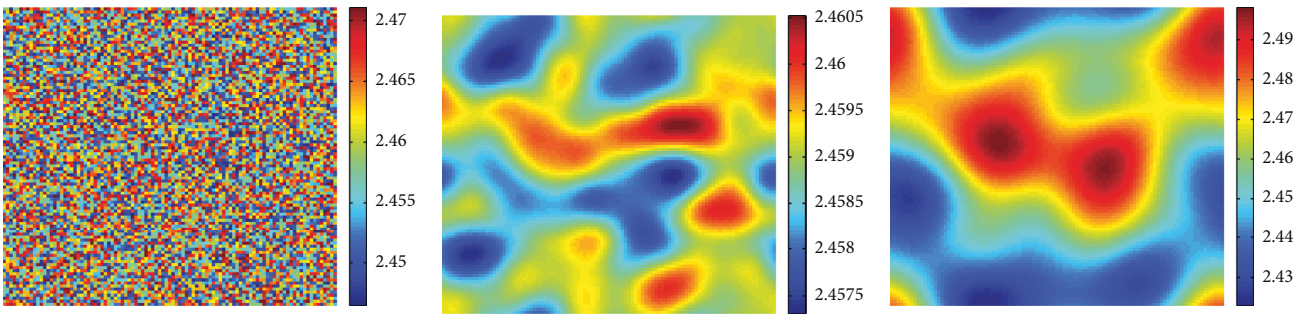

(a) (b) (c)

Figure 5: Continued.

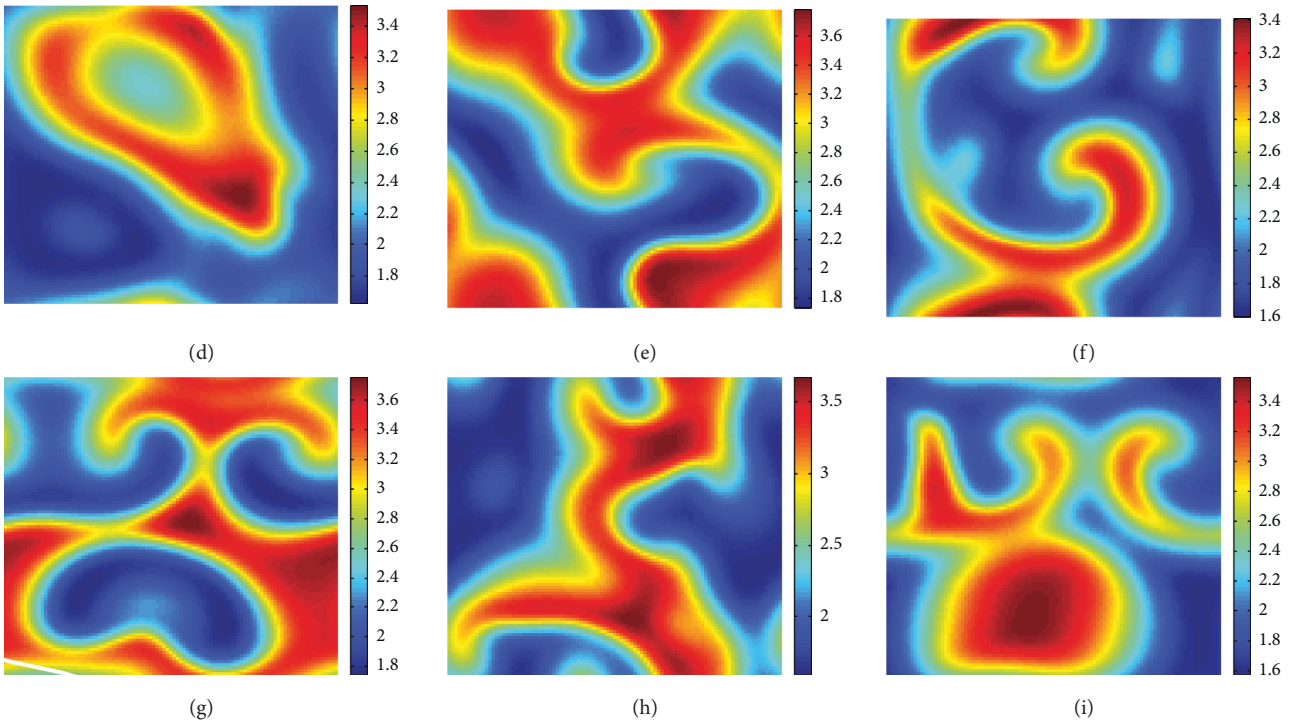

Figure 5: The process of forming cloud-like patterns over time with a time delay of 3. Parameter values: $I = 1.6$, $a = 0.5$, $b = 0.8$, $\alpha = 0.7$, $m = 0.45$, $d_1 = 0.2$, $d_2 = 0.2$, $q = 0.01$, $\tau = 3$, and $\varepsilon = 0.001$. (a) $t = 0$; (b) $t = 500$; (c) $t = 2500$; (d) $t = 5000$; (e) $t = 7500$; (f) $t = 10000$; (g) $t = 12500$; (h) $t = 15000$; (i) $t = 20000$.

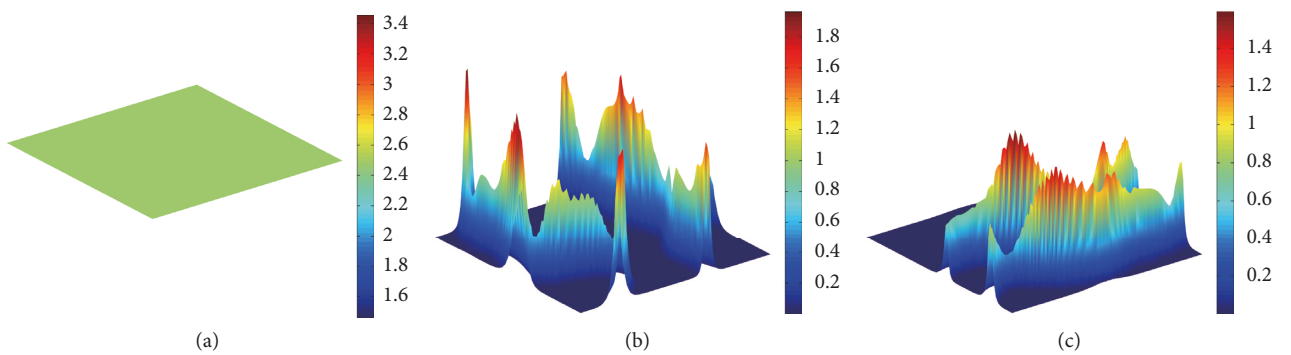

Figure 6: Spatial distribution of phytoplankton population under different diffusion parameters. Parameter values: $I = 1.6$, $a = 0.5$, $b = 0.8$, $\alpha = 0.7$, $m = 0.45$, $e = 0.2$, $h = 1$, $q = 0.01$, $\varepsilon = 0.001$, $\tau = 0$, and $t = 500$. (a) $d_1 = 1.220$, $d_2 = 0.20$; (b) $d_1 = 1.390$, $d_2 = 0.20$; (c) $d_1 = 1.389$, $d_2 = 0.21$.

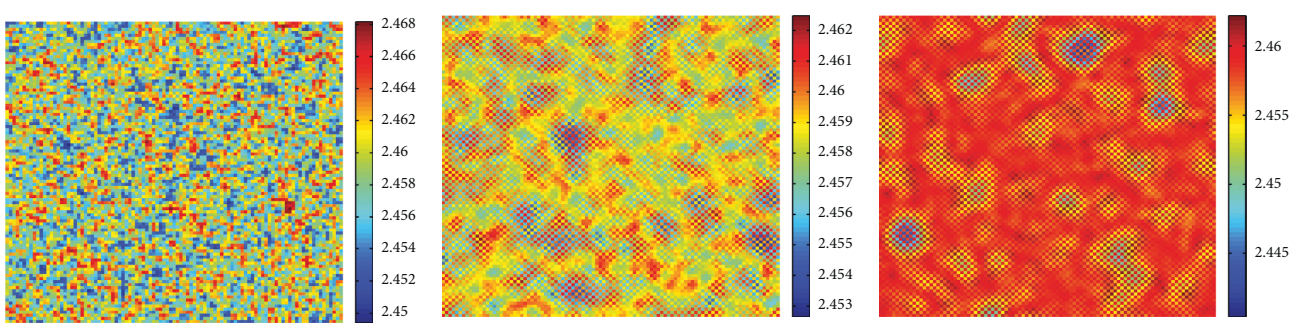

Figure 7: Continued.

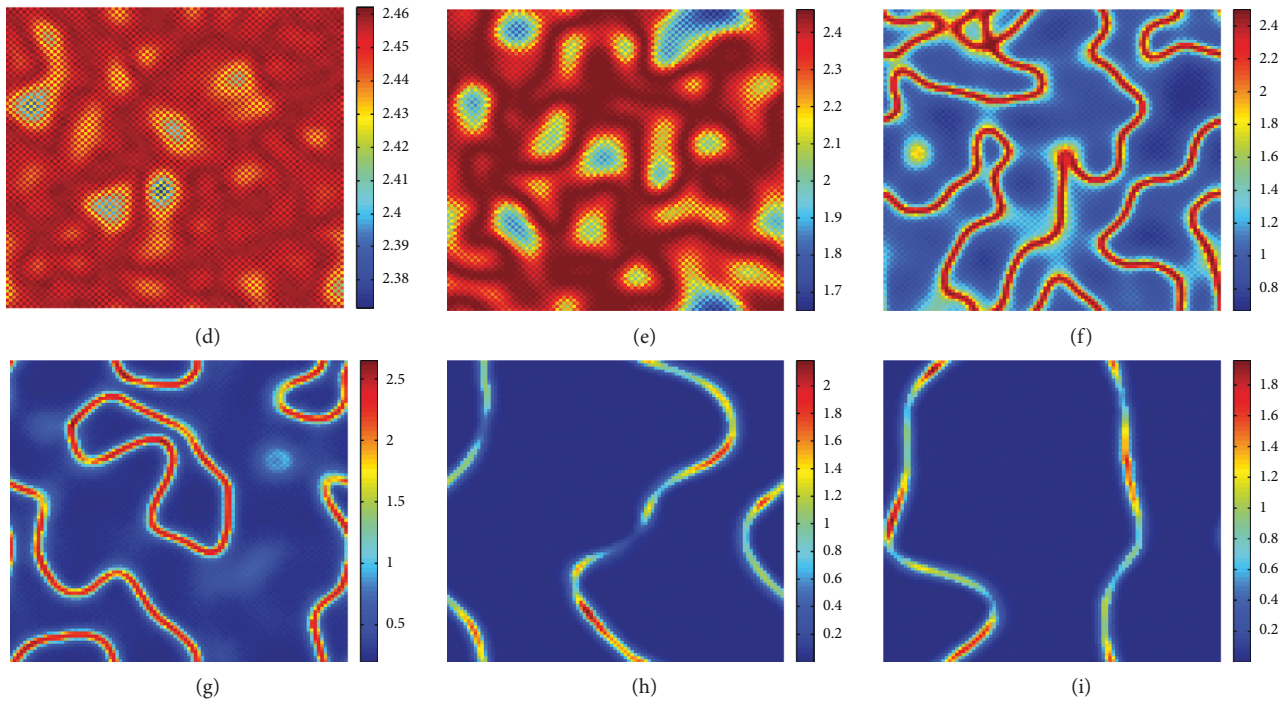

Figure 7: The formation of phytoplankton population spatial distribution pattern under certain diffusion parameters. Parameter values: $I = 1.6, a = 0.5, b = 0.8, \alpha = 0.7, e = 0.2, m = 0.45, d_1 = 1.390, d_2 = 0.20, q = 0.01, \tau = 0, h = 1$, and $\varepsilon = 0.001$. (a) $t = 5$; (b) $t = 25$; (c) $t = 30$; (d) $t = 35$; (e) $t = 40$; (f) $t = 50$; (g) $t = 100$; (h) $t = 400$; (i) $t = 500$.

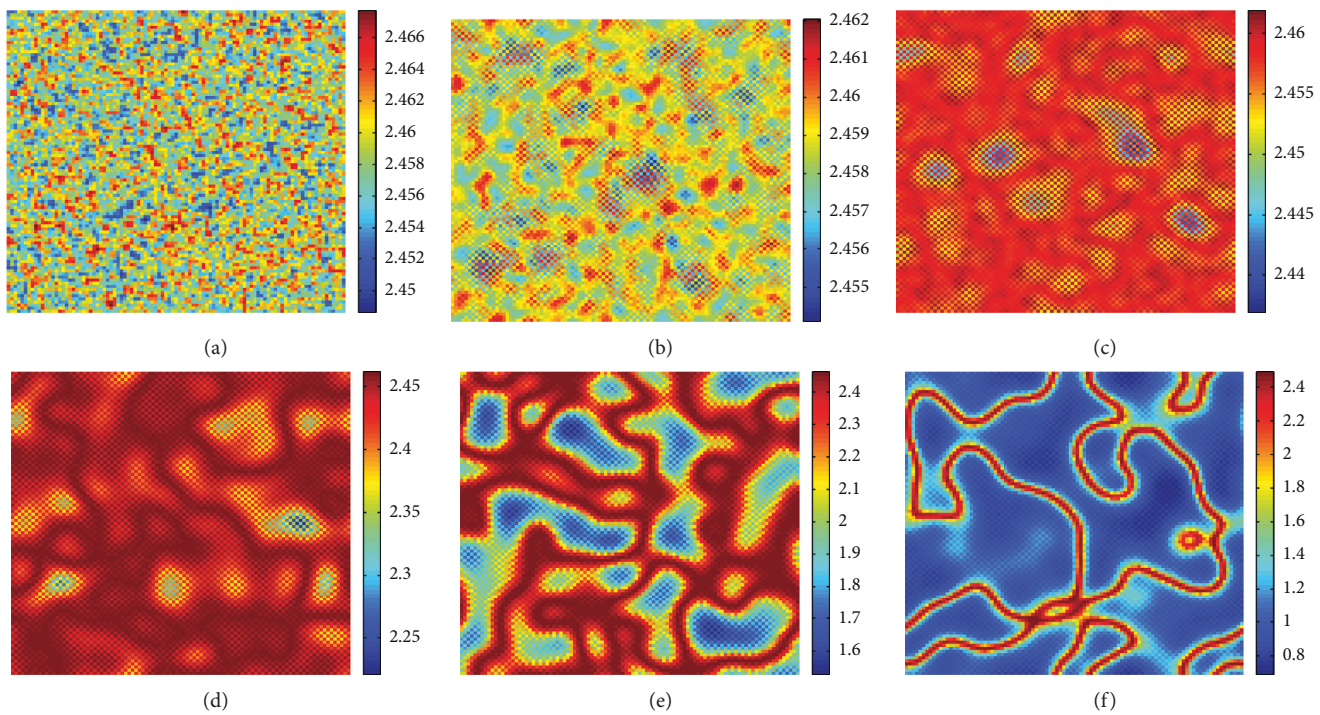

Figure 8: Continued.

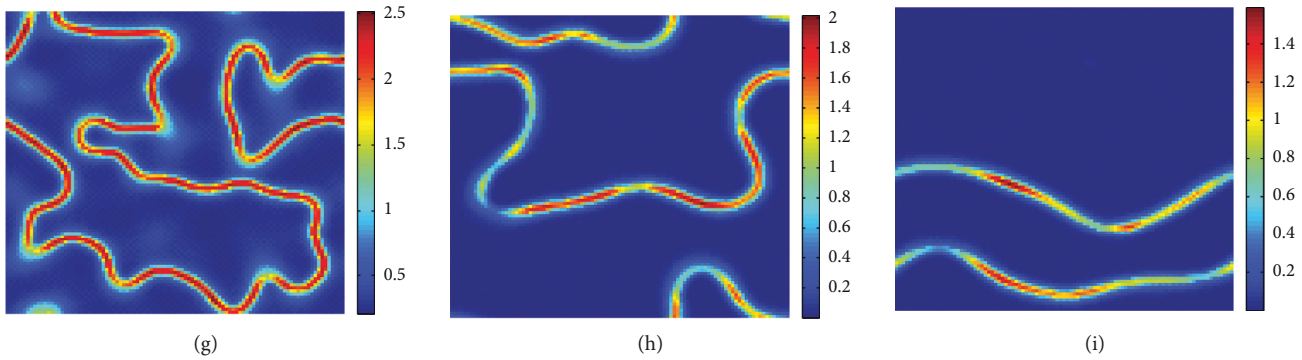

Figure 8: The formation of phytoplankton population spatial distribution pattern under certain diffusion parameters. Parameter values: $I = 1.6, a = 0.5, b = 0.8, \alpha = 0.7, e = 0.2, m = 0.45, d_1 = 1.389, d_2 = 0.21, q = 0.01, \tau = 0, h = 1$, and $\varepsilon = 0.001$. (a) $t = 5$; (b) $t = 25$; (c) $t = 30$; (d) $t = 35$; (e) $t = 50$; (f) $t = 75$; (g) $t = 100$; (h) $t = 300$; (i) $t = 500$.

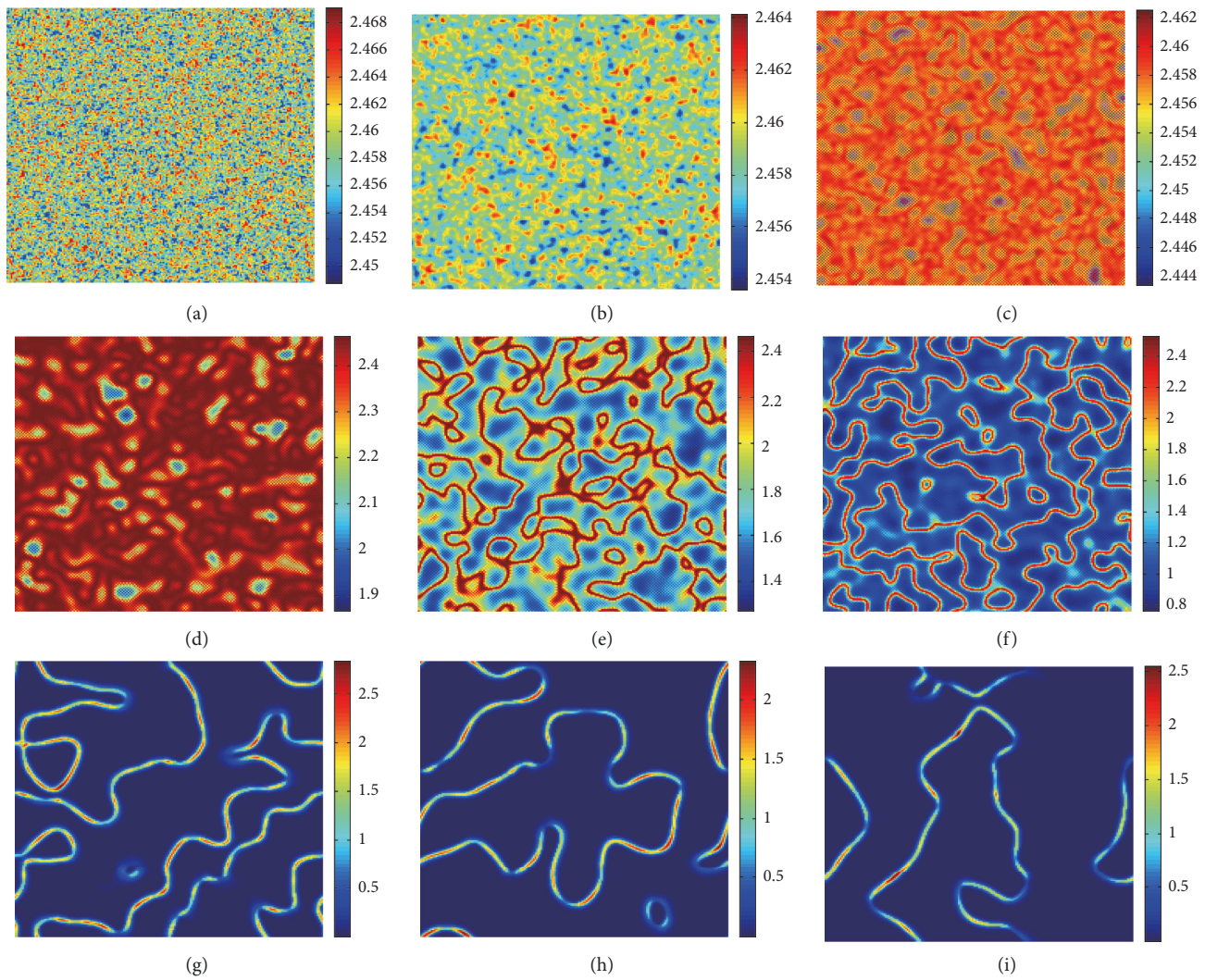

Figure 9: The formation of phytoplankton population spatial distribution pattern under certain parameters. Parameter values: $I = 1.6$, $a = 0.5, b = 0.8, \alpha = 0.7, e = 0.2, h = 1, m = 0.45, d_1 = 1.390, d_2 = 0.20, q = 0.01, \tau = 3, n = 200$, and $\varepsilon = 0.001$. (a) $t = 5$; (b) $t = 25$; (c) $t = 40$; (d) $t = 50$; (e) $t = 60$; (f) $t = 75$; (g) $t = 250$; (h) $t = 400$; (i) $t = 500$.

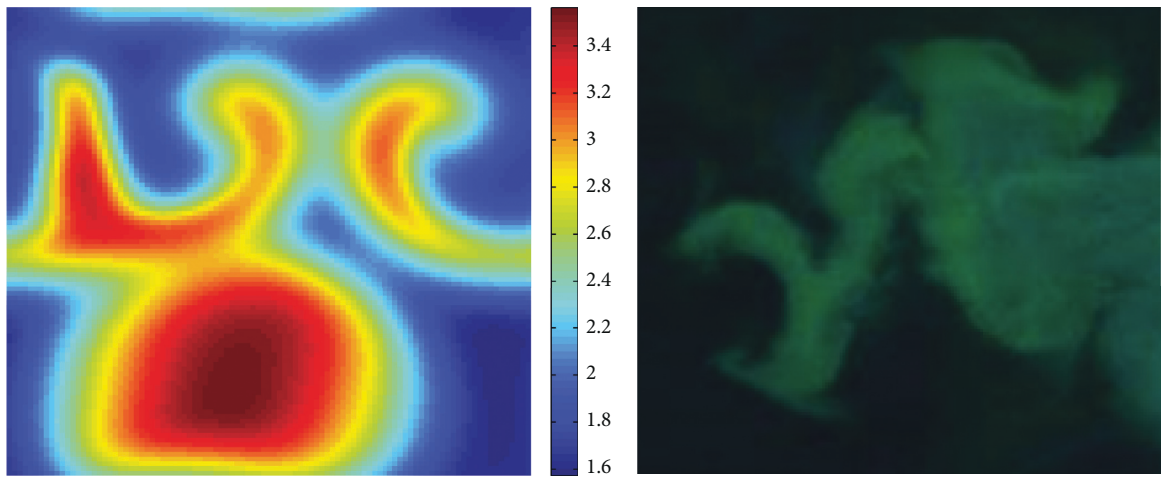

(a) (b)

Figure 10: Cloud-like patterns. Parameter values: (a) $I = 1.6$, $a = 0.5$, $b = 0.8$, $\alpha = 0.7$, $m = 0.45$, $d_1 = 0.2$, $d_2 = 0.2$, $q = 0.01$, $\tau = 3$, $\varepsilon = 0.001$, $t = 20000$, $n = 100$, $e = 0.2$, and $h = 1$. (b) On June 24, 2010, in the North Atlantic, phytoplankton was photographed on a medium resolution imaging spectrometer on NASA's "Aqua" satellite.

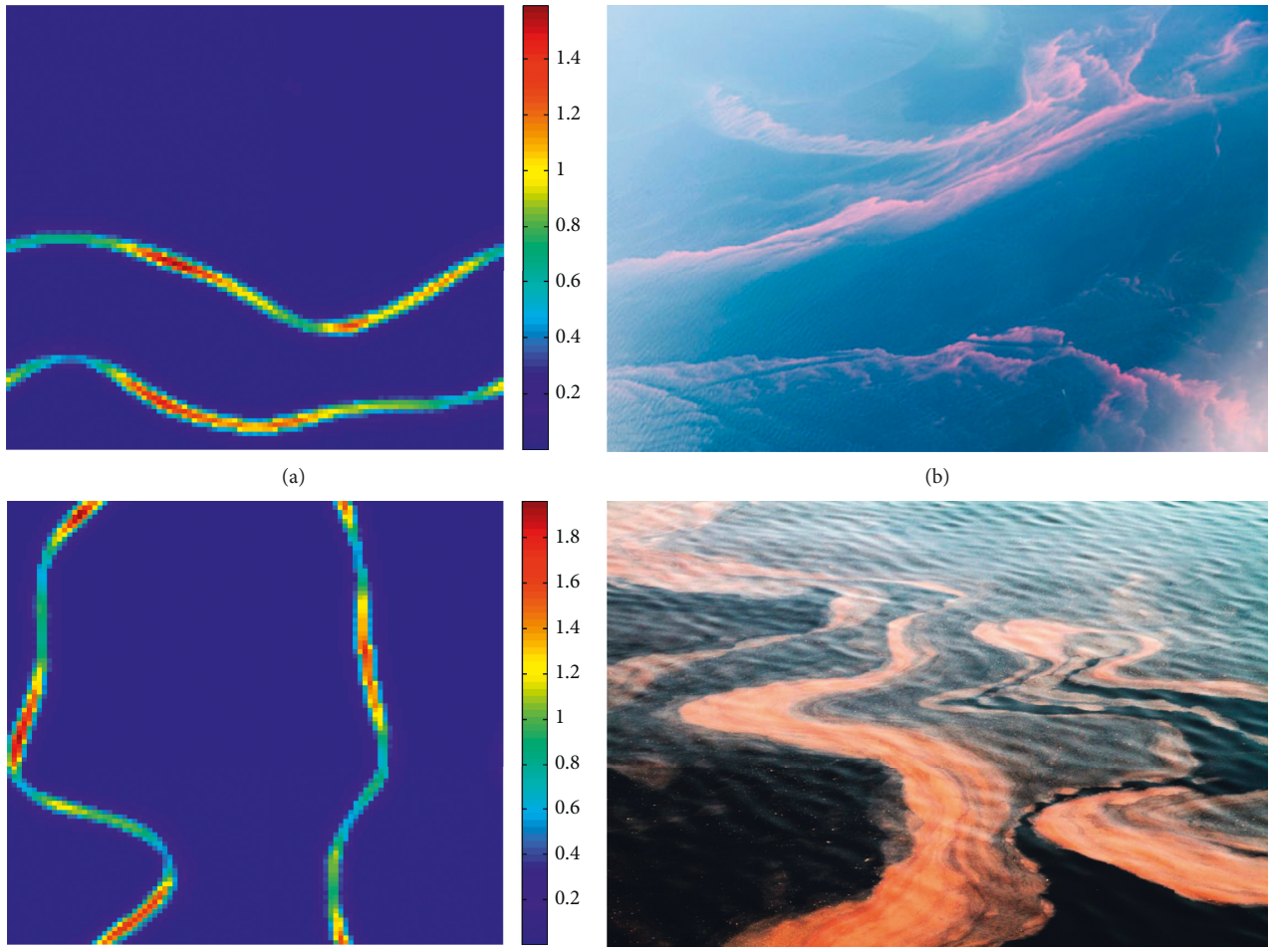

(a) (b)

(c) (d)

Figure 11: Continued.

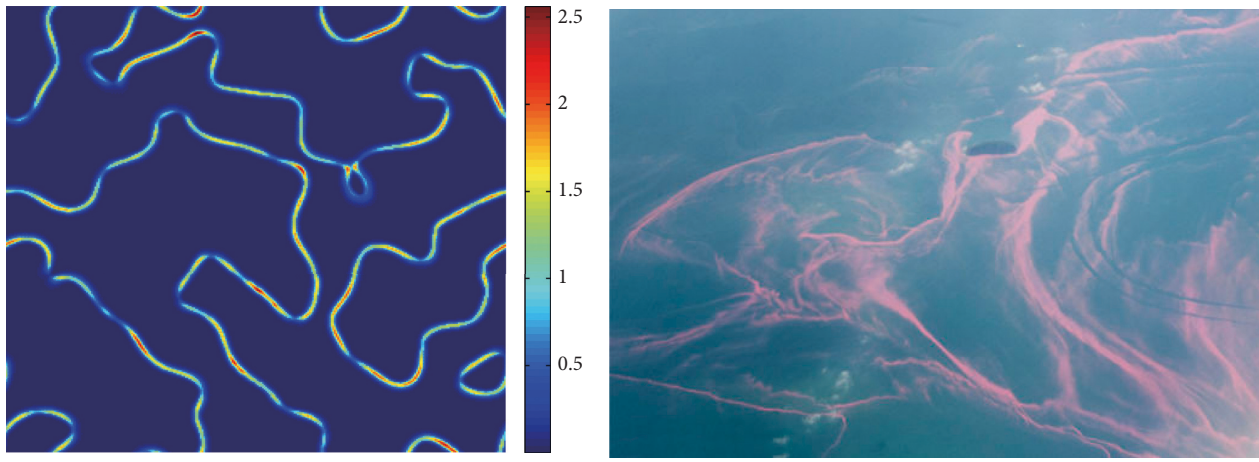

(e) (f)

Figure 11: Banded patterns. Parameter values: (a) $I = 1.6$, $a = 0.5$, $b = 0.8$, $\alpha = 0.7$, $e = 0.2$, $m = 0.45$, $d_1 = 1.389$, $d_2 = 0.21$, $q = 0.01$, $\tau = 0$, $h = 1$, $\varepsilon = 0.001$, $t = 100$, and $n = 100$. (b) On November 25, 2014, the phytoplankton bloom photographed in the sea near Shenzhen, China; (c) $I = 1.6$, $a = 0.5$, $b = 0.8$, $\alpha = 0.7$, $e = 0.2$, $m = 0.45$, $d_1 = 1.390$, $d_2 = 0.20$, $q = 0.01$, $\tau = 0$, $h = 1$, $\varepsilon = 0.001$, $t = 100$, and $n = 100$. (d) On May 7, 2012, noctilucent algae bloomed in the sea near Rizhao, Shandong, China; (e) $I = 1.6$, $a = 0.5$, $b = 0.8$, $\alpha = 0.7$, $e = 0.2$, $m = 0.45$, $d_1 = 1.390$, $d_2 = 0.20$, $q = 0.01$, $\tau = 3$, $h = 1$, $\varepsilon = 0.001$, $t = 500$, and $n = 300$. (f) On November 25, 2014, the phytoplankton bloom photographed in the sea near Shenzhen, China.

In order to show the formation process of Turing-type patterns, two sets of values are selected: $d_1 = 1.390$, $d_2 = 0.20$ and $d_1 = 1.389$, $d_2 = 0.21$. Figure 7 shows that, at the beginning, random distribution of phytoplankton starts to form a labyrinth pattern (Figures 7(b)–7(d)), and then some patches die out and form some thin stripes (Figures 7(f) and 7(g)). Finally, the number of stripes decreases over time (Figures 7(h) and 7(i)). Figure 8 shows a similar process of pattern formation with slight differences.

Note that when time delay satisfies the Neimark-Sacker bifurcation condition and coefficients d_1 and d_2 satisfy Turing bifurcation condition, simulations on pattern formation will be different. As shown in Figure 9, the general process of pattern formation is similar to that when time delay $\tau = 0$ (see Figure 7). Note that as shown in Figure 9(d) with $t = 50$, the same formation stage of patterns can be obtained in Figure 7(e) with $t = 40$. This reveals that the time delay will not change the pattern type in this situation, but will cause the delay of pattern formation stages, which is reasonable and consistent with the research of [46].

3.3. Comparison between Simulated Patterns and Real Observed Patterns. From numerical simulations, mainly two types of patterns are obtained: cloud-like patterns (Figure 10(a)) and banded patterns (Figures 11(a), 11(c), and 11(e)). Some observed patterns of phytoplankton are found and can be briefly compared with the simulated patterns from the holistic shapes. Figure 10(b) is the blooming phenomenon in the Barents Sea and shows similarity to the simulated cloud pattern (Figure 10(a)).

Figures 11(b) and 11(f) are phytoplankton bloom images taken in the waters near Shenzhen, China, in 2014, and Figure 11(d) is a large area phytoplankton bloom image of *Noctiluca scintillans* taken in the waters near Rizhao in Shandong, China in 2012. The simulated banded patterns are similar to the observed patterns. But note that we can only compare the holistic shapes or types of the patterns due to the unknown of real pattern scales, and further research should be done to explore more detailed comparison on spatial scales of the patterns.

4. Discussion and Conclusions

Through theoretical analysis and numerical simulation, the principle of space-time dynamics of phytoplankton growth and the formation process of spatial pattern distribution of phytoplankton population are explored. We mainly study the effects of time delay and, diffusion coefficients on the spatiotemporal dynamics of phytoplankton growth. The conclusions of theoretical studies and the results of numerical simulations can show that: (1) time delay τ does not affect the stability of the stable fixed point $E_0 = (I/q, 0)$, but the time delay may affect the whole process; (2) when time delay exists and is greater than a certain critical value τ_0, the time delay can not only lead to the instability of the stable fixed point E^*, but also form a cloud Neimark–Sacker pattern through Neimark–Sacker instability; (3) when $d_1 \neq d_2$, by changing the value of d_1 or d_2 to make all the eigenvalues of the diffusion term are greater than 1, then Turing bifurcation occurs. A band-shaped Turing pattern can be formed.

Both the continuous model (original model in [46]) and the discrete model in this research are reaction-diffusion models, and they have the same functional responses. The differences between the two models are as follows: in the continuous model, reaction process and diffusion process occurs at the same time, while in the discrete model, the occurring order of reaction process and diffusion process can be varied, to be exactly in this research, diffusion process

occur first and then reaction process. The main reason for us to calculate the diffusion process first is that spatial movements are quicker than reaction in the nutrient-phytoplankton system in the real world.

From the simulated patterns in this research, we can see that more complex and more types of patterns can be obtained with the discrete model than the continuous model. For example, Figure 10(a) is the simulated pattern with a similar type to the only simulated pattern in [46]. Besides, spotted, banded, and some mixed patterns are obtained in this research. This is reasonable, as Dai et al. [46] only did the Turing bifurcation. However, even with the same bifurcations, discrete models can still generate more complex patterns, due to the flexible of both time and space steps. Although continuous PDEs are still the main type of model that are used in pattern formation, many research studies on discrete dynamic systems have shown that spatiotemporal discrete models are not only more related to realistic processes but also can generate more complex dynamics [38, 39, 43, 44]. And more work could be done to explore the bifurcations induced by time step variation.

Appendix

A. Symbols Not Explained in Section 2

$$A_0 = 1 - eq - \frac{eabP^*}{(N^* + a)^2},$$

$$A_1 = 1 - em + \frac{e\alpha bN^*}{N^* + a},$$

$$A_2 = \frac{2e\alpha ab^2 N^* P^*}{(N^* + a)^3} - \frac{e\alpha ab\left(I - qN^* + 2\varepsilon mP^*\right)}{(N^* + a)^2},$$

$$B_0 = e\varepsilon m - \frac{ebN^*}{N^* + a},$$

$$B_1 = \frac{e\alpha abP^*}{(N^* + a)^2},$$

$$B_2 = \frac{e\alpha abqP^*}{(N^* + a)^2} + \frac{2e\alpha abP^*}{(N^* + a)^3}\left(I - qN^* + \varepsilon mP^*\right) + \frac{e\alpha ab^2(a - 2N^*)P^{*2}}{(N^* + a)^4},$$

$$a_{11} = 1 - eq - \frac{eabP^*}{(N^* + a)^2},$$

$$a_{12} = e\varepsilon m - \frac{ebN^*}{N^* + a},$$

$$a_{13} = \frac{eabP^*}{(N^* + a)^3},$$

$$a_{14} = 0,$$

$$a_{15} = -\frac{eab}{(N^* + a)^2},$$

$$a_{16} = -\frac{eab}{(N^* + a)^4},$$

$$a_{17} = \frac{eab}{(N^* + a)^3},$$

$$a_{18} = 0,$$

$$a_{21} = \frac{e\alpha abP^*(1 + q\tau)}{(N^* + a)^2} + \frac{2e\alpha abP^*\tau}{(N^* + a)^3}\left(I - qN^* + \varepsilon mP^*\right) + \frac{e\alpha ab^2(a - 2N^*)P^{*2}\tau}{(N^* + a)^4},$$

$$a_{22} = 1 - em + \frac{e\alpha bN^*}{N^* + a} - \frac{e\alpha ab\tau}{(N^* + a)^2}\left(I - qN^* + 2\varepsilon mP^*\right) + \frac{2e\alpha ab^2 N^* P^*\tau}{(N^* + a)^3},$$

$$a_{23} = -\frac{e\alpha abP^*(1 + 2q\tau)}{(N^* + a)^3} - \frac{3e\alpha abP^*\tau}{(N^* + a)^4}\left(I - qN^* + \varepsilon mP^*\right) - \frac{3e\alpha ab^2(a - N^*)P^{*2}\tau}{(N^* + a)^5},$$

$$a_{24} = -\frac{e\alpha ab\varepsilon m\tau}{(N^* + a)^2} + \frac{e\alpha ab^2 N^*\tau}{(N^* + a)^3},$$

$$a_{25} = \frac{e\alpha ab(1 + q\tau)}{(N^* + a)^2} + \frac{2e\alpha ab\tau}{(N^* + a)^3}\left(I - qN^* + 2\varepsilon mP^*\right) + \frac{2e\alpha ab^2(a - 2N^*)P^*\tau}{(N^* + a)^4},$$

$$a_{26} = \frac{e\alpha abP^*(1 + 3q\tau)}{(N^* + a)^4} + \frac{4e\alpha abP^*\tau}{(N^* + a)^5}\left(I - qN^* + \varepsilon mP^*\right) + \frac{2e\alpha ab^2(3a - 2N^*)P^{*2}\tau}{(N^* + a)^6},$$

$$a_{27} = -\frac{e\alpha ab(1 + 2q\tau)}{(N^* + a)^3} - \frac{3e\alpha ab\tau}{(N^* + a)^4}\left(I - qN^* + 2\varepsilon mP^*\right) - \frac{6e\alpha ab^2(a - N^*)P^*\tau}{(N^* + a)^5},$$

$$a_{28} = \frac{2e\alpha ab\varepsilon m\tau}{(N^* + a)^3} - \frac{2e\alpha ab^2 N^*\tau}{(N^* + a)^4}. \tag{A.1}$$

Data Availability

Codes related to the simulations can be made available on request (china907a@163.com).

Conflicts of Interest

The authors declare that they have no conflicts of interest.

Acknowledgments

The authors would like to acknowledge with great gratitude for the supports of the Major Science and Technology Program for Water Pollution Control and Treatment (no. 2017ZX07101002) and the National Natural Science Foundation of China (Grant nos. 11875126 and 11771140).

References

[1] D. M. Anderson, "Turning back the harmful red tide," *Nature*, vol. 388, no. 6642, pp. 513-514, 1997.

[2] Y.-H. Ahn, P. Shanmugam, J.-H. Ryu, and J.-C. Jeong, "Satellite detection of harmful algal bloom occurrences in Korean waters," *Harmful Algae*, vol. 5, no. 2, pp. 213–231, 2006.

[3] P. J. S. Franks, "Spatial patterns in dense algal blooms," *Limnology and Oceanography*, vol. 42, no. 5, pp. 1297–1305, 1997.

[4] W. Q. Chen, Q. F. Guan, C. F. Jiang, F. F. Zhang, and L. Wang, "Nonautonomous motion study on accelerated and decelerated lump waves for a $(3+1)$-dimensional generalized shallow water wave equation with variable coefficients," *Complexity*, vol. 2019, Article ID 6287461, 8 pages, 2019.

[5] A. Huppert, B. Blasius, R. Olinky, and L. Stone, "A model for seasonal phytoplankton blooms," *Journal of Theoretical Biology*, vol. 236, no. 3, pp. 276–290, 2005.

[6] M. Rehim and M. Imran, "Dynamical analysis of a delay model of phytoplankton-zooplankton interaction," *Applied Mathematical Modelling*, vol. 36, no. 2, pp. 638–647, 2012.

[7] A. Sharma, A. K. Sharma, and K. Agnihotri, "The dynamic of plankton-nutrient interaction with delay," *Applied Mathematics and Computation*, vol. 231, pp. 503–515, 2014.

[8] G.-Q. Sun, "Mathematical modeling of population dynamics with Allee effect," *Nonlinear Dynamics*, vol. 85, no. 1, pp. 1–12, 2016.

[9] X. Yu, S. Yuan, and T. Zhang, "The effects of toxin-producing phytoplankton and environmental fluctuations on the planktonic blooms," *Nonlinear Dynamics*, vol. 91, no. 3, pp. 1653–1668, 2017.

[10] F. Zhang, H. Zhang, M. R. Evans, and T. Huang, "Vegetation patterns generated by a wind driven sand-vegetation system in arid and semi-arid areas," *Ecological Complexity*, vol. 31, pp. 21–33, 2017.

[11] G. A. Riley, H. Stommel, and D. F. Bumpus, "Quantitative ecology of plankton of Western North Atlantic," *Bulletin of the Bingham Oceanographic Collection*, vol. 169, pp. 1–12, 1949.

[12] J. Monod, "The growth of bacterial cultures," *Annual Review of Microbiology*, vol. 3, no. 1, pp. 371–394, 1949.

[13] S. Babel and S. Takizawa, "Microfiltration membrane fouling and cake behavior during algal filtration," *Desalination*, vol. 261, no. 1-2, pp. 46–51, 2010.

[14] X. Bai, P. Lant, and S. Pratt, "The contribution of bacteria to algal growth by carbon cycling," *Biotechnology and Bioengineering*, vol. 112, no. 4, pp. 688–695, 2015.

[15] J. Caperon, "Population growth response of isochrysis galbana to nitrate variation at limiting concentrations," *Ecology*, vol. 49, no. 5, pp. 866–872, 1968.

[16] J. C. Goldman and E. J. Carpenter, "A kinetic approach to the effect of temperature on algal growth," *Limnology and Oceanography*, vol. 19, no. 5, pp. 756–766, 1974.

[17] J. P. Grover, "Phosphorus-dependent growth kinetics of 11 species of freshwater algae," *Limnology and Oceanography*, vol. 34, no. 2, pp. 341–348, 1989.

[18] J. P. Grover, "Resource competition in a variable environment: phytoplankton growing according to monod's model," *The American Naturalist*, vol. 136, no. 6, pp. 771–789, 1990.

[19] S. Park and Y. Li, "Integration of biological kinetics and computational fluid dynamics to model the growth of *Nannochloropsis salinain* an open channel raceway," *Biotechnology and Bioengineering*, vol. 112, no. 5, pp. 923–933, 2015.

[20] C. Ye, Z. Shen, T. Zhang, M. Fan, Y. Lei, and J. Zhang, "Long-term joint effect of nutrients and temperature increase on algal growth in Lake Taihu, China," *Journal of Environmental Sciences*, vol. 23, no. 2, pp. 222–227, 2011.

[21] E. A. Laws, S. Pei, and P. Bienfang, "Phosphate-limited growth of the marine diatom *Thalassiosira weissflogii* (Bacillariophyceae): evidence of non-monod growth kinetics," *Journal of Phycology*, vol. 49, no. 2, pp. 241–247, 2013.

[22] R. C. Dugdale, "Nutrient limitation in the sea: dynamics, identification, and significance1," *Limnology and Oceanography*, vol. 12, no. 4, pp. 685–695, 1967.

[23] L. Michaelis and M. L. Menten, "Die kinetik der invertin wirkung," *Biochemische Zeitschrift*, vol. 49, pp. 334–336, 1913.

[24] M. Latasa and E. Berdalet, "Effect of nitrogen or phosphorus starvation on pigment composition of cultured *Heterocapsa* sp," *Journal of Plankton Research*, vol. 16, no. 1, pp. 83–94, 1994.

[25] J. Arrieta, A. Barreira, and I. Tuval, "Microscale patches of nonmotile phytoplankton," *Physical Review Letters*, vol. 114, no. 12, Article ID 128102, 2015.

[26] K. Chakraborty and V. Manthena, "Modelling and analysis of spatio-temporal dynamics of a marine ecosystem," *Nonlinear Dynamics*, vol. 81, no. 4, pp. 1895–1906, 2015.

[27] S. Ghorai and S. Poria, "Turing patterns induced by cross-diffusion in a predator-prey system in presence of habitat complexity," *Chaos, Solitons & Fractals*, vol. 91, pp. 421–429, 2016.

[28] S. Ghorai and S. Poria, "Pattern formation in a system involving prey–predation, competition and commensalism," *Nonlinear Dynamics*, vol. 89, no. 2, pp. 1309–1326, 2017.

[29] L. Li, Z. Jin, and J. Li, "Periodic solutions in a herbivore-plant system with time delay and spatial diffusion," *Applied Mathematical Modelling*, vol. 40, no. 7-8, pp. 4765–4777, 2016.

[30] G. Q. Sun, C. H. Wang, L. L. Chang, Y.-P. Wu, L. Li, and Z. Jin, "Effects of feedback regulation on vegetation patterns in semi-arid environments," *Applied Mathematical Modelling*, no. 61, pp. 200–215, 2018.

[31] R. Yang, "Bifurcation analysis of a diffusive predator-prey system with Crowley-Martin functional response and delay," *Chaos, Solitons & Fractals*, vol. 95, pp. 131–139, 2017.

[32] F. Zhang, H. Zhang, T. Huang, T. Meng, and S. Ma, "Coupled effects of turing and neimark-sacker bifurcations on vegetation pattern self-organization in a discrete vegetation-sand model," *Entropy*, vol. 19, no. 9, p. 478, 2017.

[33] X. Zhang and H. Zhao, "Dynamics and pattern formation of a diffusive predator–prey model in the presence of toxicity," *Nonlinear Dynamics*, vol. 95, no. 3, pp. 2163–2179, 2018.

[34] P. Mishra, S. N. Raw, and B. Tiwari, "Study of a Leslie-Gower predator-prey model with prey defense and mutual interference of predators," *Chaos, Solitons & Fractals*, vol. 120, pp. 1–16, 2019.

[35] A. Otto, J. Wang, and R. Günter, "Delay-induced wave instabilities in single-species reaction-diffusion systems," *Physical Review E*, vol. 96, no. 5, Article ID 052202, 2017.
[36] F. A. Rihan, C. Tunc, S. H. Saker, S. Lakshmanan, and R. Rakkiyappan, "Applications of delay differential equations in biological systems," *Complexity*, vol. 2018, Article ID 4584389, 3 pages, 2018.
[37] Z. Zhang, R. K. Upadhyay, R. Agrawal, and J. Datta, "The gestation delay: a factor causing complex dynamics in gause-type competition models," *Complexity*, vol. 2018, Article ID 1589310, 21 pages, 2018.
[38] T. Huang and H. Zhang, "Bifurcation, chaos and pattern formation in a space- and time-discrete predator-prey system," *Chaos, Solitons & Fractals*, vol. 91, pp. 92–107, 2016.
[39] D. C. Mistro, L. A. Díaz Rodrigues, and S. Petrovskii, "Spatiotemporal complexity of biological invasion in a space- and time-discrete predator–prey system with the strong Allee effect," *Ecological Complexity*, vol. 9, pp. 16–32, 2012.
[40] H. N. Comins, M. P. Hassell, and R. M. May, "The spatial dynamics of host—parasitoid systems," *The Journal of Animal Ecology*, vol. 61, no. 3, pp. 735–748, 1992.
[41] X. Liu and D. Xiao, "Complex dynamic behaviors of a discrete-time predator-prey system," *Chaos, Solitons & Fractals*, vol. 32, no. 1, pp. 80–94, 2007.
[42] S. M. White and K. A. J. White, "Relating coupled map lattices to integro-difference equations: dispersal-driven instabilities in coupled map lattices," *Journal of Theoretical Biology*, vol. 235, no. 4, pp. 463–475, 2005.
[43] F. Zhang, H. Zhang, S. Ma, T. Meng, T. Huang, and H. Yang, "Self-organized patterns induced by neimark-sacker, flip and turing bifurcations in a discrete predator-prey model with lesie-gower functional response," *Entropy*, vol. 19, no. 6, p. 258, 2017.
[44] J. Wang, Y. Li, S. Zhong, and X. Hou, "Analysis of bifurcation, chaos and pattern formation in a discrete time and space Gierer Meinhardt system," *Chaos, Solitons & Fractals*, vol. 118, pp. 1–17, 2019.
[45] J. Guckenheimer and P. Holmes, *Nonlinear Oscillations, Dynamical Systems, and Bifurcations of Vector Fields*, Springer Science & Business Media, Berlin, Germany, 2013.
[46] C. J. Dai, M. Zhao, and H. G. Yu, "Dynamics induced by delay in a nutrient–phytoplankton model with diffusion," *Ecological Complexity*, vol. 26, pp. 29–36, 2016.
[47] D. Punithan, D.-K. Kim, and R. Mckay, "Spatio-temporal dynamics and quantification of daisyworld in two-dimensional coupled map lattices," *Ecological Complexity*, vol. 12, pp. 43–57, 2012.
[48] T. Huang, H. Zhang, H. Yang, N. Wang, and F. Zhang, "Complex patterns in a space-and time-discrete predator-prey model with Beddington-DeAngelis functional response," *Communications in Nonlinear Science and Numerical Simulation*, vol. 43, pp. 182–199, 2017.
[49] L. Bai and G. Zhang, "Nontrivial solutions for a nonlinear discrete elliptic equation with periodic boundary conditions," *Applied Mathematics and Computation*, vol. 210, no. 2, pp. 321–333, 2009.